Submillimeter-Wave Metrology:

Enhancement in Measurement Accuracy and Precision

A Dissertation
Presented to
the Faculty of the School of Engineering and Applied Science
University of Virginia

In Partial Fulfillment of
the Requirements for the Degree of
Doctor of Philosophy
(Electrical and Computer Engineering)

---

by

Qiang Yu

December 2015

APPROVAL SHEET

The dissertation

is submitted in partial fulfillment of the requirements

for the degree of

Doctor of Philosophy

AUTHOR

The dissertation has been read and approved by the examining committee:

Nicolas Scott Barker

Advisor

Robert Weikle

Arthur Lichtenberger

Andreas Beling

Carl Knospe

Accepted for the School of Engineering and Applied Science:

Craig H. Benson, Dean, School of Engineering and Applied Science

December

2015

Abstract

The development of terahertz (THz) frequency technology and THz integrated circuits demand more efficient and effective methods for THz measurement. Consequently, the study of THz metrology has seen rapid progress recently. In this work, two methods of using micromachined components to improve the accuracy and precision of submillimeter-wave measurement are presented. The first method focuses on improving the repeatability and reliability of terahertz probing. The principle of this method is using symmetrical integrated strain sensor pair to monitor and control the contact condition of terahertz on-wafer probe. This method improves the repeatability of terahertz probing and enables accurate contact force measurement without modification to the standard probe station. Repeatable RF measurements can be achieved by aligning the probe tips angularly and controlling the contact force using the integrated strain sensors. Taking advantage of this technique, measurement uncertainty of THz probing can be characterized. In addition, the recommended probe station specifications and procedure for THz probing without any integrated strain sensor are provided. The second method focuses on improving the accuracy of calibration by improving the quality of calibration standards (quarter-wave calibration shims). Microfabricated calibration shims for the WR-2.2 band were fabricated and tested. The corner radii effect can be greatly reduced, which enables the fabrication of geometrically complex waveguide components, such as waveguide twist.

Acknowledgement

Firstly, I would like to thank my academic advisor, Dr. N. Scott Barker, for his guidance, inspiration, encouragement and support throughout my doctoral studies at the University of Virginia. He has been, is, and will always be a role model for me in my research work as well as other aspects. I would also like to thank Dr. Robert Weikle II and Dr. Arthur Lichtenberger, who I consider my co-advisors. I would like to express my appreciation for my dissertation committee members, Dr. Andreas Beling and Dr. Carl Knospe for their valuable advice.

This work would not be possible without the help and support of my fellow members at the University of Virginia. I would like to take this opportunity to thank Matthew Bauwens, Huilin Li, Lihan Chen, Theodore Reck, Chunhu Zhang, Huihui Wang, Defu Liang, Jian Zhang, Jie Wang, Alex Arsenovic, Robert Benoit, Angelique Sklavounos, Chenqian Gan, Jiguang Li, Jiaxing Guo, James Do, Sami Hawasli, Naser Alijabbari, Michael Cyberey, Joseph Beatrice, Alex Lobo, Harry Wade, and Tim Pernell. I would also like to thank Dr. Jeffrey Hesler at Virginia Diode and Dr. Anthony Kerr at National Radio Astronomy Observatory for their help.

Finally my love and gratitude goes to my wife, Dr. Linlin Li, my daughter, Abigail Yu, my father, Professor Xiaoping Yu, and my mother, Li Li, for all their support and patience over the years. They were the original impetus for me to go through graduate school.

Contents

1 Introduction to Terahertz Technology Application

The development of terahertz (THz) frequency technology has recently drawn great attention and seen rapid progress. In this work, we focus on the submillimeter-wave region of the electromagnetic spectrum. Typically, the submillimeter-wave frequencies range from 300 GHz to 3 THz, of which the corresponding wavelengths range from 1 mm to 0.1 mm, located between traditional microwave and optical frequencies (as shown in Figure 1.1) [1]. Emergence of powerful sources and ultra-sensitive detectors operating in this frequency range enable an increasingly wide variety of applications such as spectroscopy [2], imaging and sensing [3], medical detection [4], radio astronomy [5], communication [6], manufacturing [7], global environmental monitoring [8], etc.

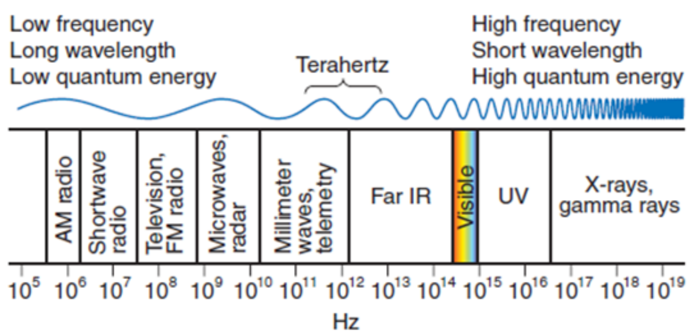

Figure 1.1: The electromagnetic spectrum [1].

1.1 THz Spectroscopy

THz spectroscopy is a rapidly evolving field. It not only is an important tool in metrology, but also provides the foundation for many other THz applications such as imaging, medical detection, industrial quality control, global environmental observation, etc. Numerous gases and organic solids show distinct absorption features in the THz range. The spectrum can be acquired using either time-domain (pulsed) [9] or frequency-domain (continuous-wave) radiation [10]. Comparing the spectrum of THz radiation through or reflected by the sample under test with the reference spectrum enables the characterization of materials. In addition to the transmission and reflection type spectroscopy, other detection geometries have been developed, such as attenuated total reflection [11]. Figure 1.2 shows the schematic of a THz time-domain spectroscopy system. The refractive index and absorption coefficient of the sample are analyzed based on the temporal shapes of the reference pulse and measured pulse (transforming into frequency domain). Future development includes further expand the applications of THz spectroscopy, the development of ultrabroadband THz spectroscopy, reducing the cost of THz spectroscopy system, increasing the data processing speed, reducing the complexity of the system [2].

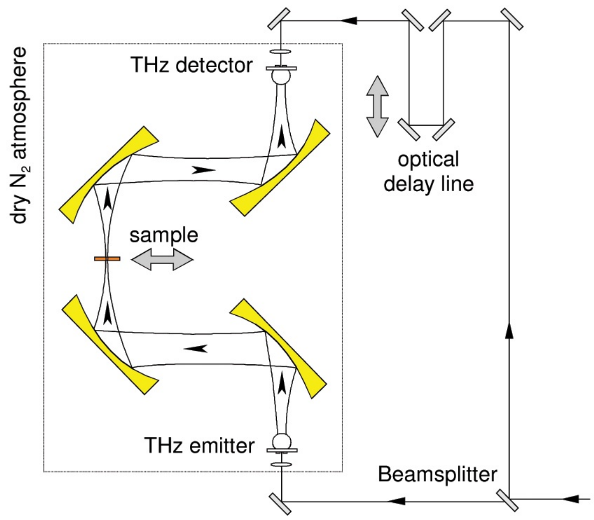

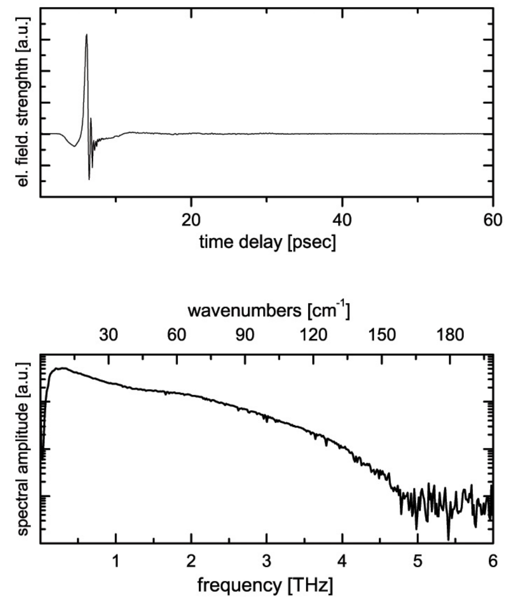

Figure 1.2: (a) Schematic diagram of a THz time-domain spectrometer. (b) Temporal shape of a THz-pulse and corresponding frequency spectrum [12].

1.2 Imaging and sensing

Three prime motivations promote the imaging and sensing applications of THz technology: (a) THz radiation is readily transmitted through most non-metallic, non-polar materials, enabling the detection beyond concealing barriers. (b) Target compounds including explosives and chemical or biological agents have characteristic THz spectra that can be used for identification. (c) THz radiation poses minimal health risk for the scanning of human body. Information such as chemical data or image can be extracted from the reflected or transmitted radiation. Figure 1.3 shows the potential implementation of the THz imaging system in transmission mode and reflection mode [3]. An image system with standoff distance of 25 m has been reported in 2010 [13]. Passive THz imaging system with 5 m standoff distance has been reported in 2014 [14]. Recent work demonstrates the formation of 3-D image using synthetic aperture radar (SAR) techniques [15]. The major limitations of THz imaging and sensing includes the lack of high power sources and compatible low-noise receivers to overcome the attenuation loss in humid atmosphere and barrier media, especially for standoff detection [3].

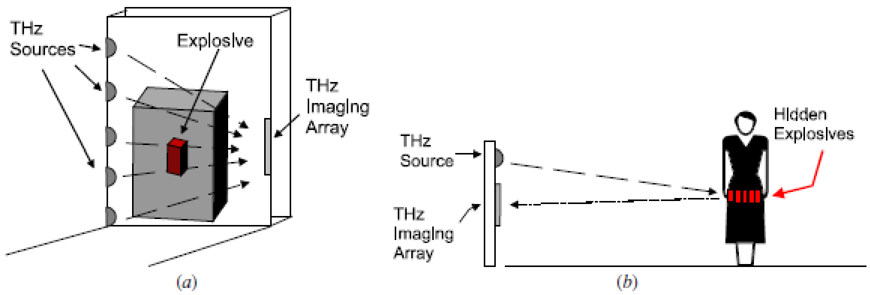

Figure 1.3: Illustration of potential implementation of a THz imaging array in transmission mode (a) and reflection mode (b) [3].

- Biomedical detection -

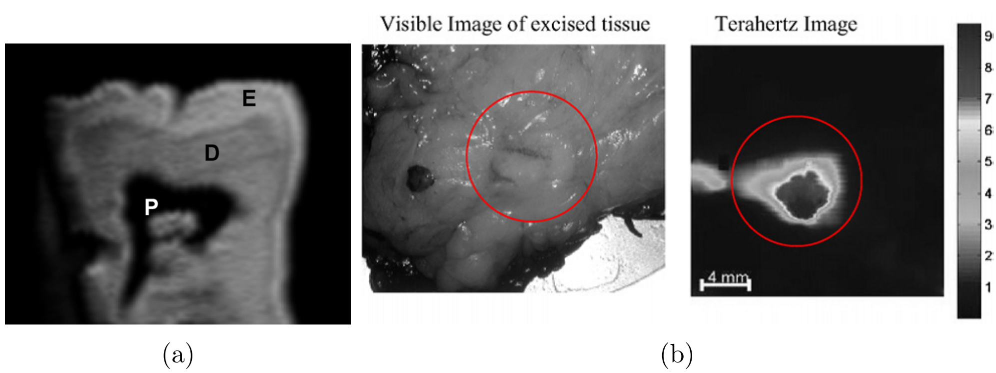

Figure 1.4: (a) an image of a human tooth; (b) Mastectomy specimen with an invasive lobular carcinoma (circled) [16].

Due to the low energy of THz photons, THz scanning causes minimal or no damage to the molecules of scanned object, making it ideal for both in-vivo and ex-vivo biomedical examination. Small molecules can be identified by the characteristic absorption spectrum and large molecules are usually identified by the transmission and phase change of THz waves. Different types of cells or different states of the same cell feature different responses to THz waves. This phenomenon can be widely utilized in clinical diagnostics, such as skin cancer detection [17], breast cancer detection and dental imaging as shown in

Figure 1.4a and 1.4b [4]. Additionally, THz hydration sensing enables utility in the diagnostic and study of burn and ophthalmology [18]. THz blood spectroscopy enables in-vivo tissue differentiation during surgical procedure [19]. Recent work found the correlation of electro-cardiogram parameters and the sub-THz reflection coefficient of human skin opens the gate to remote cardiac monitoring [20].

1.3 Radio astronomy

The THz portion of the electromagnetic spectrum is one of the most harboring spectral signatures of ions, atoms and molecules. Ground-based, airborne and space THz astronomy instrumentation facilitate observations to examine molecular clouds and dark cloud cores, which promote our understanding of the composition and origin of the solar system, the evolution of matter in our galaxy and the star formation history of galaxies over cosmic timescales [5], [21]. Taking advantage of the outstanding sensitivity, THz superconducting receivers are widely used in astronomy applications [22]. Figure 1.5 shows the antennas at the Atacama Large Millimeter/submillimeter Array (ALMA).

Figure 1.5: Antennas at Atacama Large Millimeter/submillimeter Array (ALMA).

1.4 THz communication

Taking advantage of the higher frequency and broader information bandwidth than microwave, THz communication has the potential of achieving data rate in tens of gigabits per second. However, severe atmospheric attenuation limits its applications to shorter ranges (such as indoor communications systems). The initial prospective usages are similar to indoor communication systems such as wireless local area network (WLAN) or wireless personal area network (WPAN). The ultimate goals include expanding the operating distance of THz devices and building cost effective THz integrated circuits. In addition, secure battle field wireless system can take advantage of the high directivity of THz beams, which makes it hard to intercept [6]. The Interest Group THz has been established within The Institute of Electrical and Electronics Engineers (IEEE) 802.15 to create standards for various THz communication systems [23]. Figure 1.6 shows the technology road map of THz communications [24].

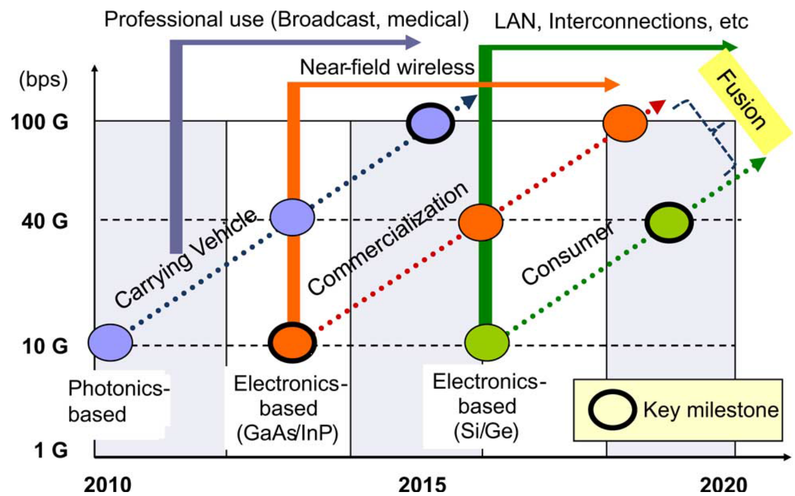

Figure 1.6: Technology road map of THz communications [24].

1.5 Manufacturing

Manufacturing quality control systems in a variety of industries can benefit from the new possibilities offered by THz technology. The fact that certain materials are transparent to THz waves enables non-destructive exam of agricultural, pharmaceutical and food products. A primitive THz imaging system detecting defects or undesired elements for industrial quality control has been demonstrated by D. Etayo, et al. (shown in Figure 1.7) [7]. Several commercialized products of non-destructive testing using THz waves have been developed in recent years.

1.6 Global environmental monitoring

The overview of the THz remote sensing is given in Figure 1.8 [8]. The spectroscopic response of many biological and chemical compounds are distinctive in the THz range, presenting tremendous potential in environmental monitoring of atmospheric chemical compositions and the identification of climate evolution in the troposphere and lower stratosphere [25]. THz earth environmental observation systems have been developed to monitor

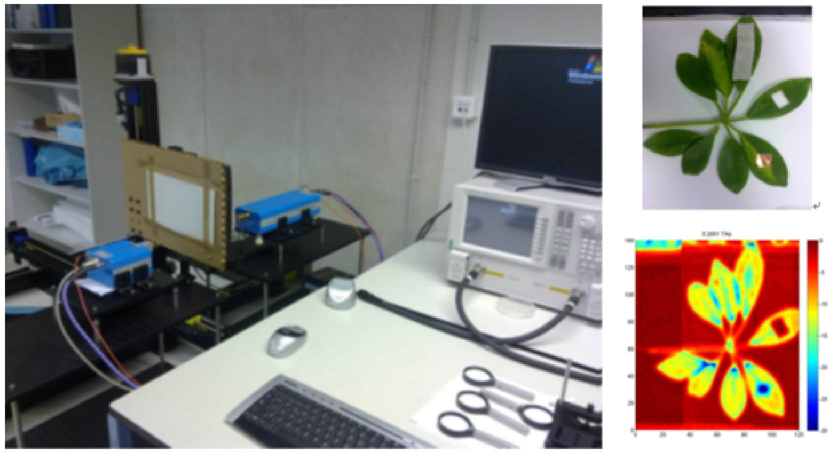

Figure 1.7: A THz imaging system [7].

different substances [26], [27]. Atmospheric propagation models of THz waves in different kinds of climate conditions are yet to be constructed for remote sensing as well as many other applications including communication and secure imaging.

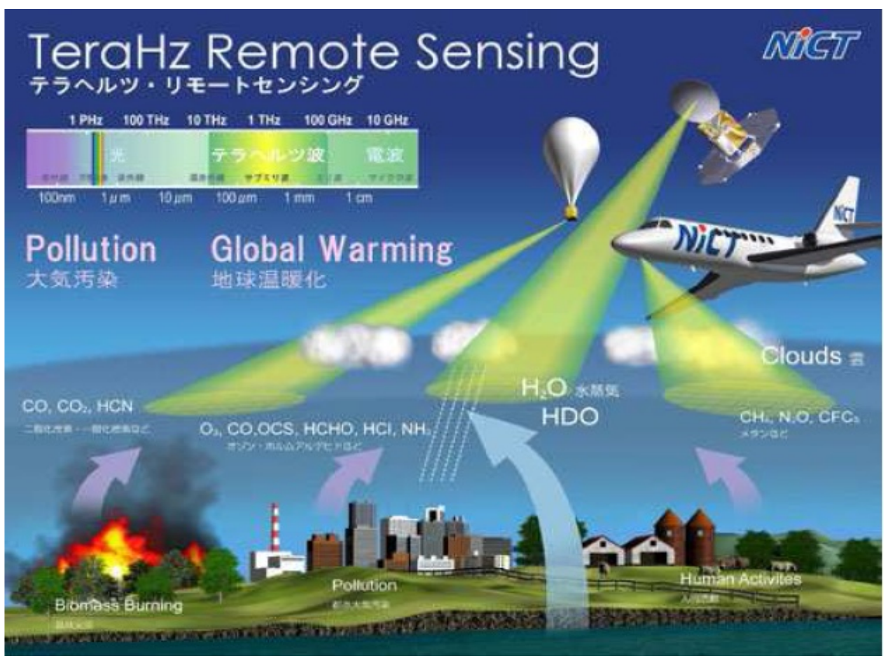

Figure 1.8: THz remote sensing techniques [8].

Though recent breakthroughs, especially in THz sources, detectors, systems and application-oriented achievements [28], [29], pushed THz research into the center stage, the cost, size, weight and complexity of existing terahertz systems limit its application and development. For many potential applications such as THz sensor networks, confidential satellite communication, weatherproof monitoring systems among others, higher-power sources, more sensitive sensors, innovative functional devices and materials are yet to be developed [28]. Prominent improvement in THz circuit and component technologies are needed. Development in THz metrology in the past few years, especially in on-wafer measurements [30], [31], provides more accurate methods of characterizing THz circuits, which will significantly benefit the THz devices research.

2 Integrated Strain Sensor for Micromachined Terahertz Probe

2.1 Terahertz Integrated Circuits

Integrated circuits can effectively reduce the cost, size, and weight of THz components. Significant progress has been made in the last decade to push operating frequencies of integrated circuits well into the submillimeter wave range [28]. Lai et al. demonstrated a 35 nm indium phosphide (InP) high-electron-mobility transistor (HEMT) device (T-gate) with Fmax greater than 1 THz (extrapolated due to equipment limitation) in 2007 [32]. Deal, et al. demonstrated a cascode 30 nm InP HEMT amplifier with 10 dB gain at 550 GHz operating frequency in a split-block waveguide housing package in 2010 [33]. In 2012, a multi-stage InP HEMT amplifier with a peak gain of approximately 30 dB at 670 GHz was reported [34]. Submillimeter-wave Schottky diodes also have been developed vigorously in recent decades. A 2.5 THz monolithic gallium arsenide (GaAs) diode mixer has been reported in 1999 [35]. In 2013, GaAs based Schottky diode fabricated on silicon (Si) was first been demonstrated [36]. In 2014, the operating frequency of this type of device has been pushed to 1.1 THz [37]. The THz electronics program of the Defense Advanced Research Projects Agency (DARPA) has set the current goal to develop high performance THz integrated circuits that operate at center frequencies exceeding 1.0 THz. With ongoing transistor scaling efforts, both frequency and performance of THz integrated circuits are expected to increase in the near future.

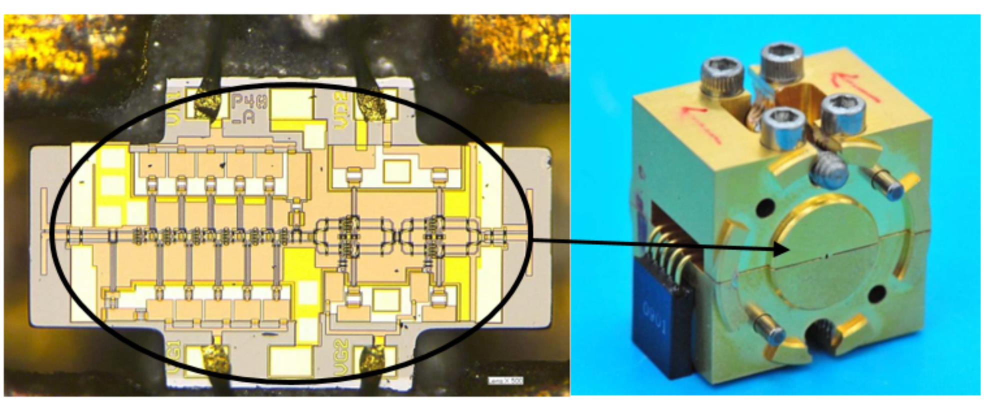

Figure 2.1: A typical submillimeter-wave circuit test setup [38].

2.2 Terahertz Device Measurement

With the advance in submillimeter-wave monolithic integrated circuits (S-MMICs), the testing of S-MMICs has evolved rapidly in recent years. Previously, tests of S-MMICs were performed in a waveguide block that held the circuit chip and had corresponding waveguide flanges at each port. As an example, a typical test fixture of a submillimeter-wave circuit is shown in Figure 2.1 [38]. The amplifier chip shown had to be etched out from a larger wafer into individual pieces, placed in a waveguide block and connected to DC signal pads. This process features several drawbacks listed (but not limited to) below:

- The assembling process is highly time consuming and requires lots of training to perform properly.
- The performance of the circuit depends on the accuracy of the assembly. To accurately de-embed the test fixture is difficult, if not impossible.
- The testing is destructive. Not only can the chip not be reused after being dismounted from the waveguide block, certain positions of the waveguide block will also be worn over time.

Different methods for THz testing have been developed to address the above problems. These methods can be summarized into two categories - non-contact methods and on-wafer probing methods.

2.2.1 Non-Contact Terahertz Measurements

Since 2012, a group at the Ohio State University has published several papers on the topic of non-contact measurements for device testing at THz frequencies based on radiative coupling of vector network analyzer (VNA) test ports to the coplanar waveguide (CPW) of THz ICs via planar, on-chip antennas. [31, 39–41]. Figure 2.2 shows the non-contact probe test setup. The on-chip antennas act as "virtual" probe tips and connect to the device under test (DUT) through CPW lines. The DUT must be integrated with planar THz antennas and measurement signals are transmitted from VNA test ports through a quasi-optical link [41]. The proof-of-concept demonstration was done in WR-2.2 (325 GHz

- 500 GHz) and WR-1.5 (500 GHz - 750 GHz) bands with greater than 12 dB reported insertion loss. The authors claim that this technique can be scaled beyond 900 GHz, but have not validated the argument. From a metrology point of view, the repeatability of non-contact probing is yet to be studied. The test setup is complex and delicate compared to contact probing, but the insertion loss is comparable. Figure 2.3 shows the scattering parameters (S-parameters) of the non-contact probe (between the VNA test port and the calibration reference plane).

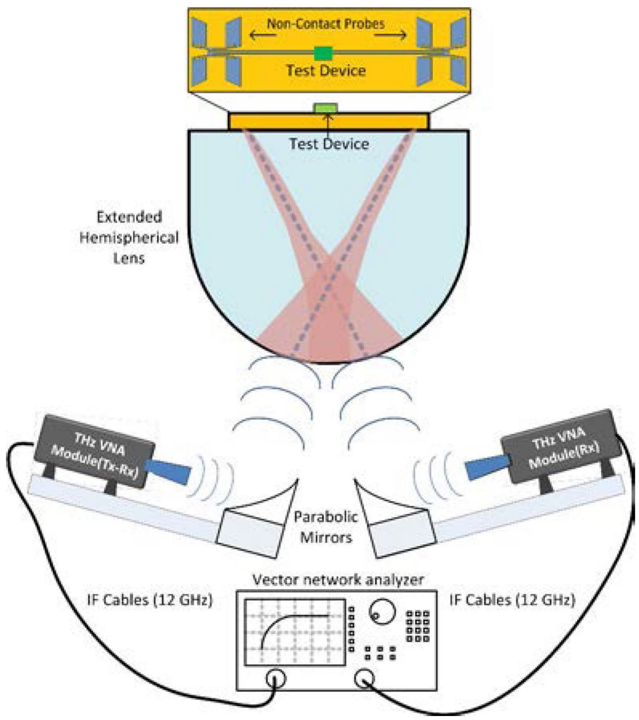

Figure 2.2: Non-contact probe test setup [41].

Another non-contact THz measurement system which is capable of measuring multiport devices using a two-port VNA was developed at the University of Michigan [42]. It couples a small fraction of the signal at each waveguide port to free space using a reflection-canceling slot array. The signals are measured by an open-ended waveguide probe and then used to calculate the S-parameters of the DUT. Figure 2.4 shows the schematic of the multi-port S-parameter measurement technique. Even though measurement repeatability close to on-wafer probing can be achieved with this technique, its applications are limited by the configuration.

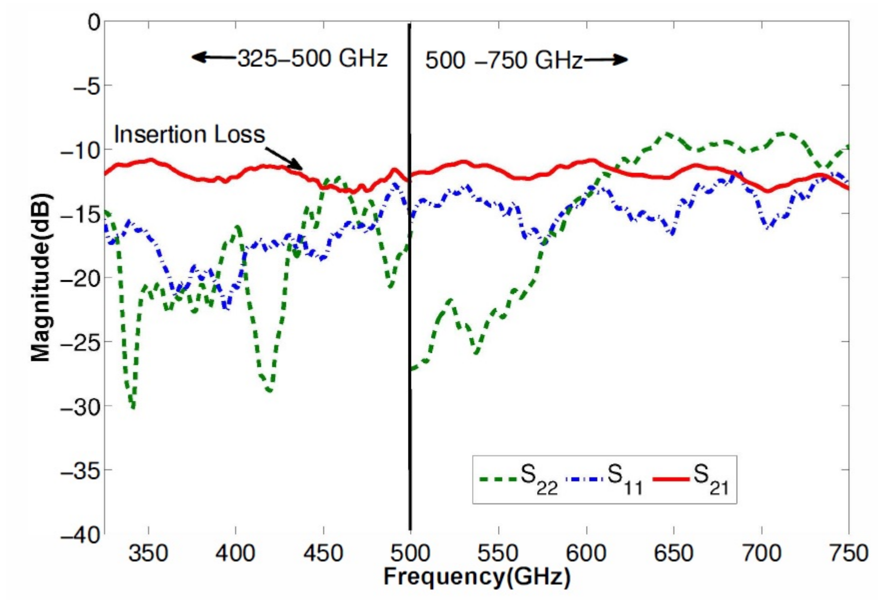

Figure 2.3: Non-contact probe S-parameters [41].

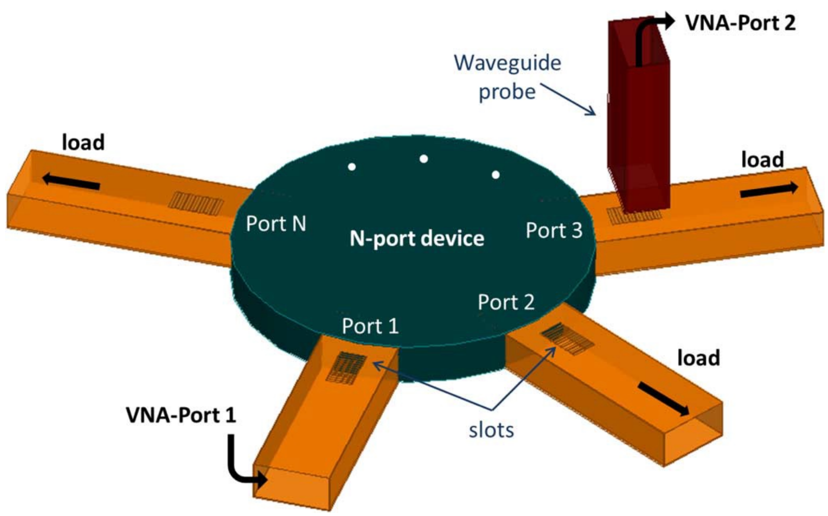

Figure 2.4: Schematic of multiport S-parameter measurement technique [42].

2.2.2 Terahertz On-Wafer Measurements

Inspired by what is done at lower frequencies, on-wafer probing operating in THz frequencies has been developed by our group (T. Reck, et al.) since 2010 [43], [30]. Figure 2.5 shows a probe test setup [44]. The micromachined probe chip is housed in an E-plane split-waveguide metal-machined block and the probe tip extends 400 μm beyond the metal housing. The probe assembly adopts a similar configuration as the S-MMICs. WR-1.2 (600 GHz - 900 GHz) probes were demonstrated in 2012 [45]. WR-1.0 (750 GHz - 1.1 THz) probes were first introduced in 2014 [46]. All the micromachined THz probes are recently made commercially available by Dominion Microprobes Inc. (DMPI) [47].

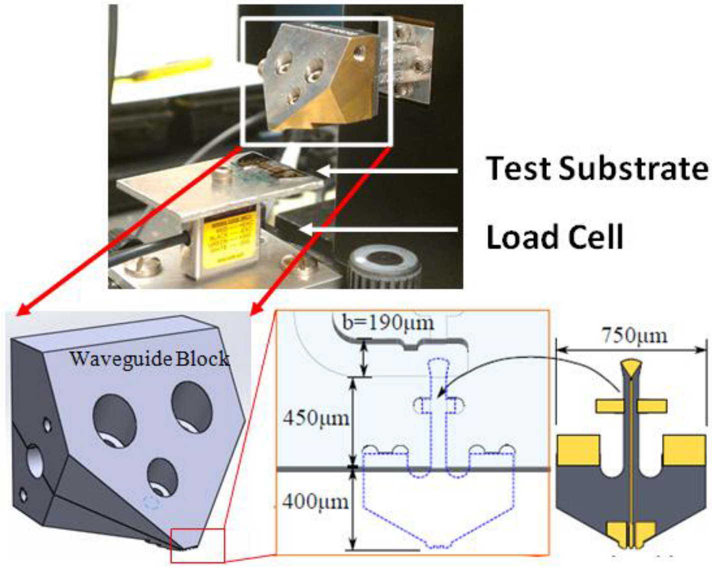

Figure 2.5: Micromachined THz on-wafer probe test setup.

Using on-wafer probing, the effort and cost to characterize a large number of devices can be significantly reduced. More importantly, this method provides more insight to the testing process: accurate calibrated on-wafer measurements are enabled by eliminating errors and effects associated with waveguide test fixtures; the die can be sorted by performance; the yield of the wafer can be decided, etc.

As shown in Figure 2.5, the probe terminates in CPW to form Ground-Signal-Ground (GSG) tips. In order to achieve accurate measurement, all tips must contact the test substrate with sufficient force which requires approximately 1 mN per tip for a constant resistance $< 0.1\ \Omega$ according to experimental results [43]. In previous work, a load cell has been used to control the contact force [44]. This method provides no information regarding the probe contact angle, i.e., whether the probe tips are parallel to the test substrate (shown in Figure 2.6a). One method to solve this issue is to apply excessive contact force to ensure all tips are contacting the test substrate simultaneously (previous work used 20 mN contact force [44]). However, this causes uneven mechanical wear at the probe tips, unnecessarily heavy scratch marks on the die, and reduced probe lifetime. In certain semiconductor fabrication technologies, extensive probing is necessary through the whole process. The reduced probe lifetime and scratch marks will increase cost due to longer delivery time and reduced yield. A scanning electron microscope (SEM) image of a tilted probe with uneven mechanical wear is shown in Figure 2.6b. Additionally, it is difficult to incorporate a load cell with the standard probe station, which may require significant modification to the test system.

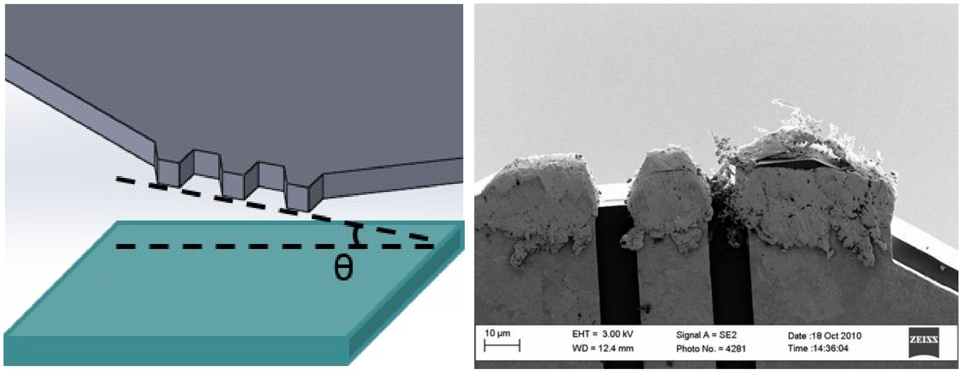

(a) (b)

Figure 2.6: (a) Demonstration of an angularly misaligned probe contacting the test substrate with contact angle θ. (b) SEM image of the micromachined probe tips with uneven mechanical wear.

To solve the planarization issue, a primitive angular alignment is performed prior to taking data by observing scratch marks the probe tips made on the wafer, and adjusting the probe contact angle until the scratch marks are even. After the initial angular alignment, the probe still needs to be overdriven to ensure that all three tips are contacting the test substrate with sufficient force. The probe tips still suffer from excessive wear which can cause reduced lifetime. Therefore, harder materials such as nickel [46] or cobalt hardened gold (99.7 % purity) [44] have been used at the probe tips to extend probe lifetime. In that case, potential damage to the circuit under test which reduces yield is still a problem. In addition, to accurately adjust the planarization, DC resistance measurement on the two ground tips proves sufficient but requires significant die area for the test structure.

Previous work by our group has shown that using the primitive angular alignment and overdriving the probe provides acceptable accuracy and precision [44]. In metrology research or cases where high measurement repeatability is required, an alternative method to monitor and control the probe contact for contact force and planarization is desired.

2.3 Integrated Strain Sensor for Probe Contact Detection

In this work, an improved method using integrated strain sensors for monitoring and controlling the contact condition of terahertz on-wafer probes is developed. This method utilizes the mechanics of wafer probing shown in Figure 2.7. When the probe contacts the test substrate, the probe chip deflects and generates a force at the contact point which depends on the probe material properties, probe shape, probe angle and the relative movement between the probe and test substrate/stage.

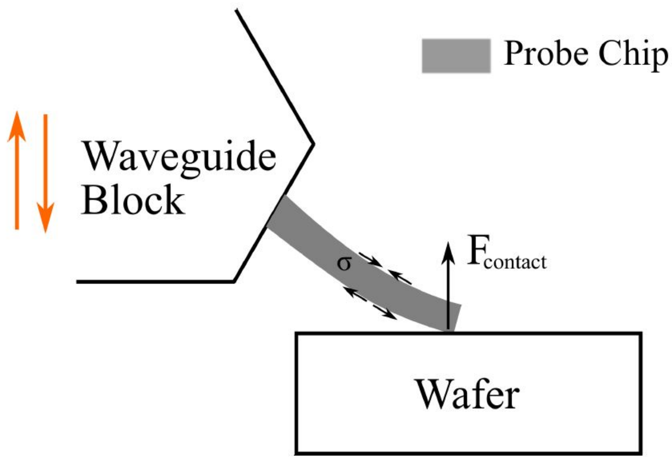

Figure 2.7: The mechanism of wafer probing [48].

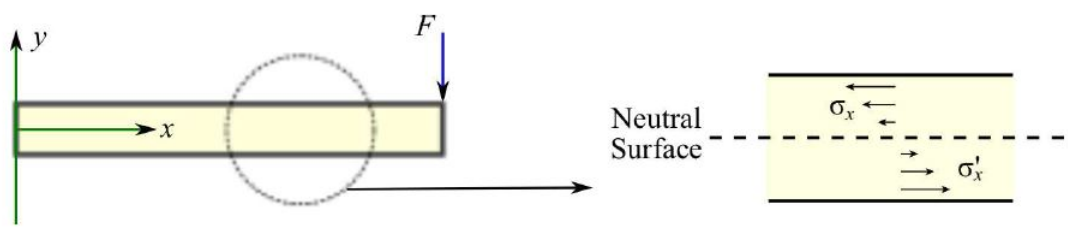

Figure 2.8: Side view of a cantilever beam under point load with one end fixed [48].

The classic cantilever model can be used for an initial analysis [48], [49]. The wafer probing mechanism is very similar to the bending of a cantilever beam under point load with one end fixed. When a force is applied at the free end of a cantilever beam, the beam will deflect. Stress is generated due to the deflection. Figure 2.8 shows the side view of a cantilever beam under point load with one end fixed and the stress in the cross section (x-y plane) of the beam. The axial stress at the top surface of the beam can be calculated by the following equation [50],

$$\sigma_x(x) = \frac{6F(L-x)}{wt^2} \tag{2.1}$$

where F is the force. L, w, t, and x are the length, width, thickness of the beam, and the distance to the fixed end, respectively. E is the Young's modulus of the beam material. The axial strain associated with stress $\sigma_x(x)$ can be expressed as

$$\varepsilon_x(x) = \frac{\sigma_x(x)}{E}. \tag{2.2}$$

When the probe is contacting the test substrate with angular misalignment, the strain is larger on the side that makes the contact first. In this case, a cantilever beam under a torsional loading can be used to analyze the mechanical behavior of the probe. Section 2.3.4 contains a more detailed explanation.

The principle of our method is that angular misalignment between the probe tips and the test substrate generates asymmetrical strain on symmetrical positions of the probe. Strain sensors placed symmetrically can measure the strain generated by the deformation of the probe during contact and can be used to determine the angle of misalignment. The probe angle can be adjusted according to the outputs of the strain sensors. In addition, once angularly aligned, the strain sensors can be used to sense the probe contact force, which serves as a substitution for the load cell. The benefits of using strain sensors include:

- *Accurate contact force measurement without modification to the standard probe station.* Repeatable probe contact force is crucial for RF measurement repeatability and can be achieved by properly monitoring and controlling the strain generated at designated positions on the terahertz probe due to probe deformation during probe contact. Inconstant contact force causes variation in the probe skating, which introduces phase error in the measurement.

- *Detect angular misalignment.* In addition to eliminating the need for a load cell to monitor vertical contacting force, this method has the ability to detect angular misalignment by sensing asymmetrical strain on symmetrical positions of the probe. Angularly aligned (to the test substrate) probes enhance measurement accuracy and repeatability, require much lower contact force, extend probe lifetime, and make less impact on the device under test.

- *No additional on-wafer circuitry.* This method is also advantageous over measuring the probe tip contact resistance with required additional on-wafer circuitry.

- *Enhanced measurement repeatability on large wafers.* This method is especially beneficial for probing on large wafers where the wafer thickness profile may vary by 5 to 10 μm. Such variation can lead to 3 to 6 mN variation in contact force for a probe with 0.65 mN/μm spring constant [44] given a fixed z-travel. With current probe station designs, it is difficult to make repeatable contact across the whole wafer due to the wafer thickness profile variation.

- *Measurement uncertainty characterization on large wafers.* Three factors contribute to the on-wafer measurement uncertainty, including contact force variation, stage accuracy and repeatability, and source uncertainty. Taking advantage of the strain sensor's accurate contact force control, the contact force variation can be eliminated from the measurement uncertainty, which enables quantitative analysis of each factor.

2.3.1 Sensor Type and Material

Strain sensors based on different principles are reviewed and compared in Table 1. Resistive strain sensors are the most efficient in terms of sensitivity, fabrication complexity and test set up complexity. The dominant factor in the resistance change is deformation of the metal thin film. Semiconductor strain sensors based on the change in resistivity have higher sensitivity and a similar test setup, but require several additional fabrication steps and usually have worse temperature stability [51]. Hence, in this application, ductile metal is chosen as the sensor material.

Additionally, the temperature dependence of electrical resistivity of the sensor material, characterized by the temperature coefficient of resistance (TCR), needs to be taken into account. Table 2 lists the TCR of selected metals and metal alloys [57]. As shown in Table 2, nickel chromium alloy (NiCr) is less sensitive to temperature variation than most other materials, which enables more accurate measurement. Thus, for the sensor material, evaporated NiCr (80-20 wt.%) which is a common material for strain sensing is used [58,59]. NiCr films with different compositions have been reviewed. Previous work has shown that 80-20 wt.% is the optimal choice in terms of temperature stability, resistivity, and sensitivity

Table 1: Comparison between selected types of strain sensors.

Sensor type	**Dominant principle**	**Sensitivity**	**Fabrication complexity and cost**	**Test set up complexity**
Optical [52]	Fiber Bragg grating	Varies, generally high	Low	High
MEMS resonant [53, 54]	Tuning fork, capacitive, etc.	Comparable to silicon sensors	High	High
Carbon nano tube (CNT) [55]	Piezoresistivity of CNTs	Gauge factor below 6	Medium	Low
Magnetic shape memory alloy (MSMA) [56]	Martensitic reorientation	Generally for large strain sensing	High	High
Semiconductor thin film [51]	Piezoresistivity of material	Gauge factor 20 - 200	Medium to high (depending on material)	Low
Metal and metal alloy thin film [51]	Deformation of thin film resistor	Gauge factor below 5	Low	Low

[60]. Other suitable materials include constantan (copper nickel alloy, 55-45 wt.%) and manganing (copper manganese nickel alloy, 86-12-2 wt.%).[1]

2.3.2 Probe Design and Simulation

The THz probe chip with integrated strain sensor in this work is a modified design of the micromachined WR-1.5 probe with bias capability designed by DMPI [47]. A detailed in-block view of the probe chip is illustrated in Figure 2.10. Both the low-pass filter and waveguide transition including waveguide step and radial stub are redesigned to remove the low-end resonance and improve insertion loss and return loss [44], [47]. All the probe chips are fabricated using a 15 μm silicon on insulator (SOI) wafer. As shown in the probe test setup (Figure 2.5), the probe chip is housed in an E-plane split-waveguide metal-machined block and the probe tip extends 400 μm beyond the metal housing (shown in Figure 2.9). It connects to the test port of a VNA extension module through a rectangular waveguide flange machined in the block. There is approximately 1 inch of rectangular waveguide built in the

[1]The benefit of using material with ultralow TCR such as constantan or manganing is insignificant due to the metal film resistor ($\pm$0.0001 TCR) in the testing bridge circuit. NiCr provides sufficiently low sensitivity to temperature.

Table 2: List of the TCR of selected metals and metal alloys [57].

Metal	Temperature coefficient of resistance (K^{-1})
Aluminum	0.0039
Copper	0.0039
Constantan	0.00001
Gold	0.0034
Iron	0.0050
Lead	0.0039
Manganing	0.000002
Mercury	0.0009
NiCr	0.0004
Nickel	0.0060
Platinum	0.0039
Silver	0.0038
Tin	0.0045
Tungsten	0.0045
Zinc	0.0037

metal block between the waveguide flange and the backend of the probe chip (the radial stub). The probe terminates in CPW to form GSG tips. The probe chip is self-aligned by recesses machined in the waveguide block and clamped by compressing electroplated gold on both sides of the chip to provide mechanical support. Two additional DC bias channels are milled on the meal block to measure the outputs of the integrated sensors. The electroplated gold clamped during probe chip assembling is also used as ground for both sensors. An important feature of this design is that devices such as strain sensors can be easily integrated with the probe due to the current probe fabrication process.

The probe with integrated strain sensors are fabricated as shown in Figure 2.11. A lift-off process with e-beam evaporation is used to deposit the NiCr thin film. Photoresist AZ5214 is used to define the sensor area as well as the alignment markers for the following steps. NiCr is evaporated at the deposition rate of 0.15 nm/s to desired thickness using an e-beam evaporator. After deposition, the AZ5214 is removed by soaking in Acetone for 15 minutes. A detailed description of the probe fabrication process for step (b) through (i) can be found in [48].

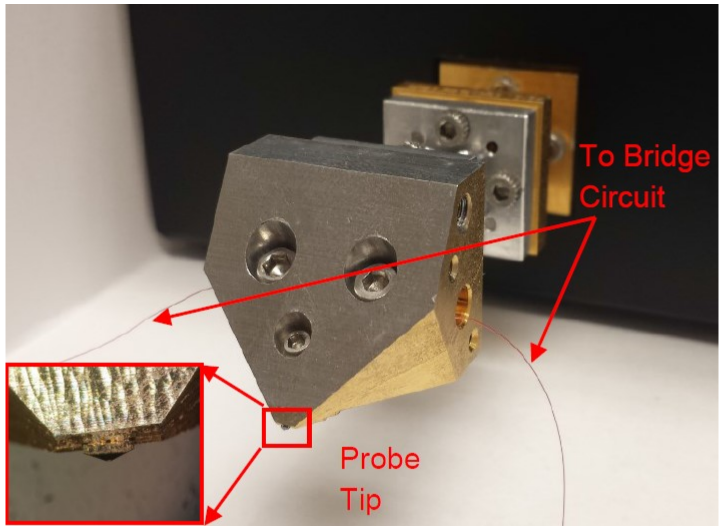

Figure 2.9: Photograph of the assembled probe.

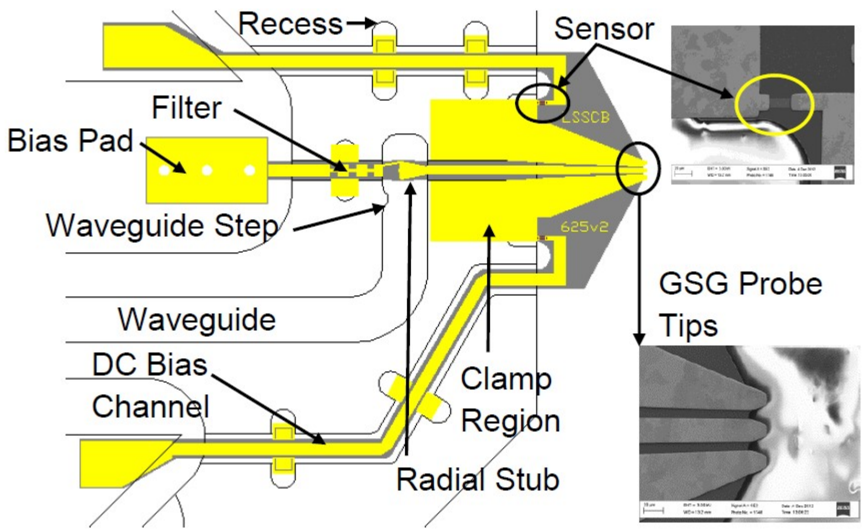

Figure 2.10: In-block view of the probe chip.

Figure 2.12 shows the simulated strain distribution profile of the WR-1.5 probe with 20 mN contact force using ANSYS 14.0. The dimensions used in the simulation are shown in Figure 2.13. Silicon is used as the probe beam material (density 2330 kg/m^3, Young's modulus 185 GPa, Poisson's ratio 0.278, shear modulus 52 GPa). The clamped areas are set to be fixed and point loads are applied to the probe tips. All three tips are assumed to contact the test substrate simultaneously. The NiCr strain sensor is positioned on the probe to ensure maximum angular sensitivity as well as minimum interference to the RF signal. The optimization of the sensor position will be discussed in the follow sections.

Figure 2.14 shows the high frequency structural simulator (HFSS) simulation results

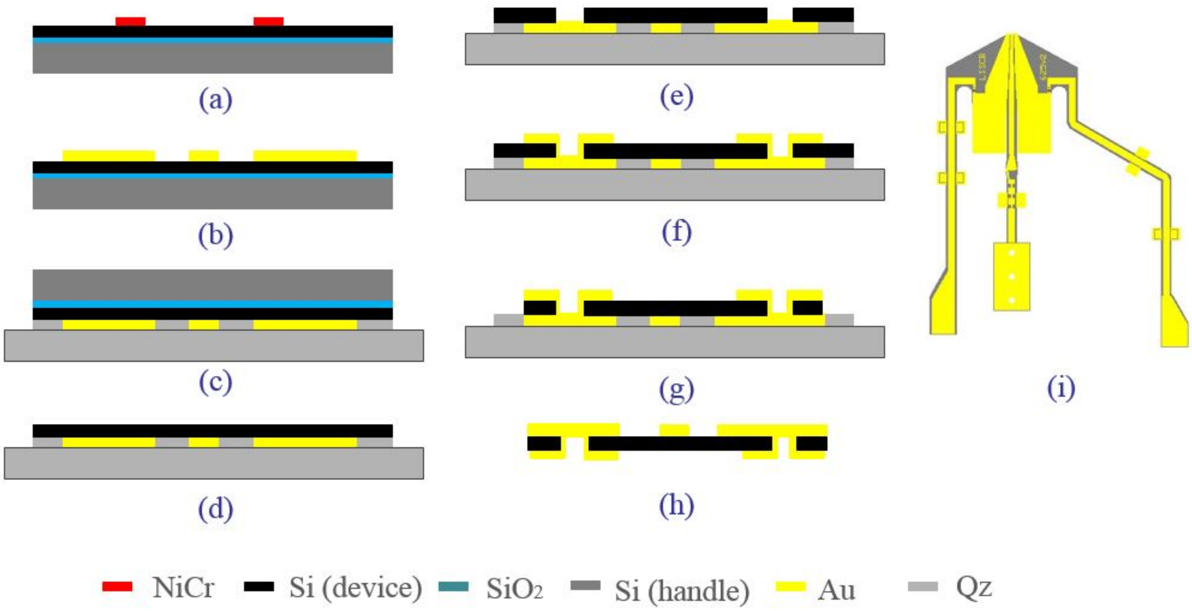

Figure 2.11: Process flow for the probe chip. (a) Define the NiCr layer using lift-off process. (b) Define the beam-layer on SOI wafer by electroplating. (c) Mount the SOI wafer upside down to a quartz wafer. (d) Remove handle silicon and insulator layer. (e) Etch through-substrate via. (f) Metalized via holes and define bottom metal layer. (g) Define the extend of probe chips by reactive-ion etching (RIE) etching. (h) Cross-sectional view of a finished and released probe chip. (i) Top view of a finished probe chip.

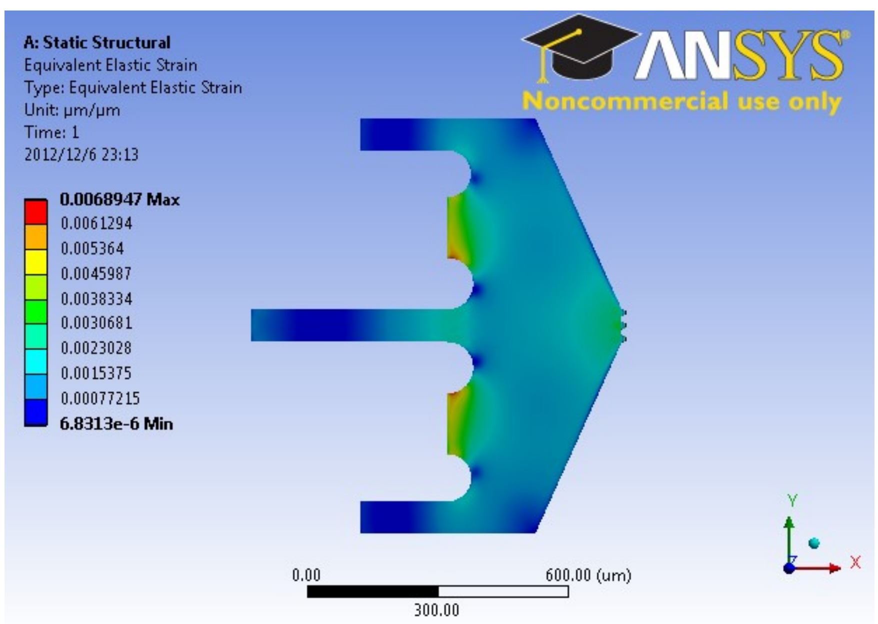

Figure 2.12: Simulated strain distribution profile of WR-1.5 probe with 20 mN contact force (ANSYS 14.0).

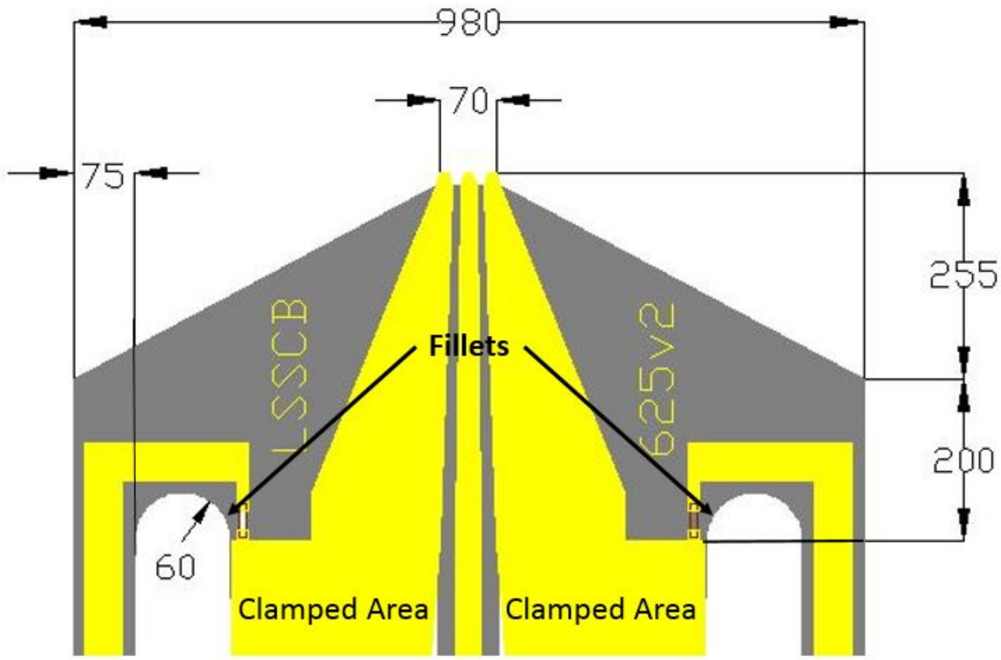

Figure 2.13: Dimensions of the WR-1.5 probe used in the mechanical simulation. Unit: μm

of the S-parameters (magnitude) of the probe assembly. In simulation, both the 1 inch waveguide built in the metal block and the probe chip are included. Waveguide surface roughness is set to 200 nm and metal (Au) conductivity is set to 3.1×10^7 S/m [61].

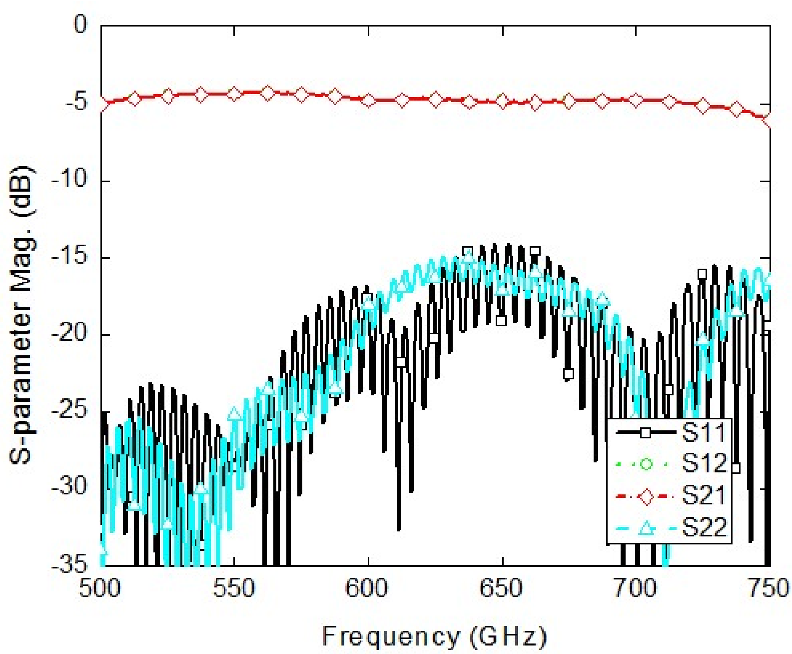

Figure 2.14: HFSS simulation results for WR-1.5 probe (HFSS 14.0).

2.3.3 Resistance Calculation

As can be seen from Figure 2.12, the strain at different locations of the probe varies. Hence, the strain at different locations of the sensor, which is a thin film resistor, varies accordingly. The actual response of the sensor, i.e., the resistance of the sensor under stress, needs to be calculated. In this section, a method to calculate the resistance of the strain sensor is introduced.

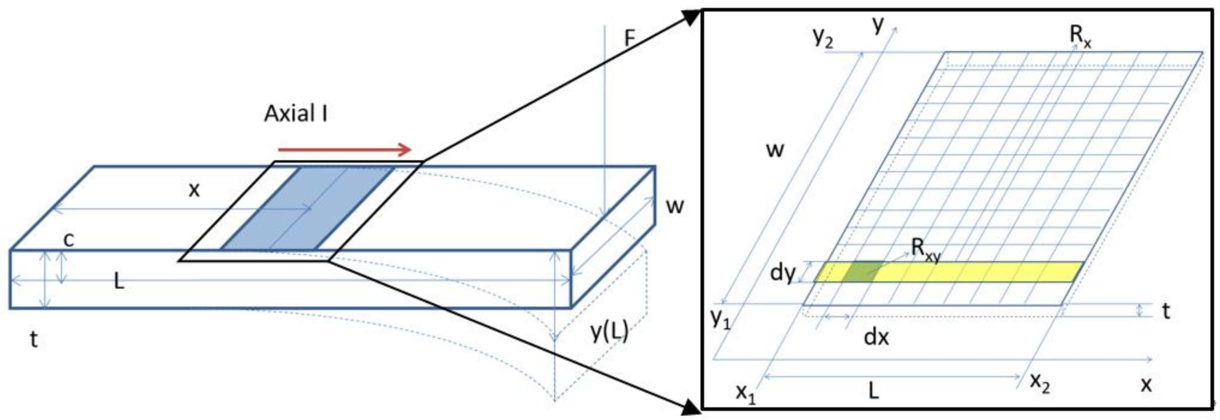

Figure 2.15: Diagram for sensor resistance calculation.

The principle of this calculation is demonstrated in Figure 2.15. The rectangular sensor can be divided into smaller elements (rectangles), so that the strain is assumed to be uniform in each element. The resistance of each element can be calculated based on the strain within this area. Accumulating the resistance of all elements gives the total response of the sensor to a certain stress. Current is applied to the sensor along the direction (x) of stress in Figure 2.15. All the elements in each row are in series and can be combined into one resistor (marked yellow). All the combined resistors are in parallel across y direction. The following derivation shows the detail of the resistance calculation. The resistance R of a rectangular resistor with axial current is

$$R = \rho \frac{L_f}{w t_f} \tag{2.3}$$

where L_f, w, t_f denote the length, width and thickness of the resistor (film) and ρ is the resistivity of the sensor material (width of the beam equals width of the resistor in this example). Assuming axial stress is applied to the sensor, taking the derivative on both sides gives

$$\frac{dR}{R} = \frac{d\rho}{\rho} + \frac{dL_f}{L_f} - \frac{dw}{w} - \frac{dt_f}{t_f} \tag{2.4}$$

Where $\frac{dL_f}{L_f}$, $\frac{dw}{w}$ and $\frac{dt_f}{t_f}$ denote the axial (ε_{xf}), transverse (ε_{yf}) and vertical strain (ε_{zf}). From [62], the axial strain for a prismatic cantilever beam is

$$\varepsilon_{xf} = \frac{6F(L-x)}{E_b w t_b^2 (1 + \frac{E_f t_f}{E_b t_b})} \tag{2.5}$$

where F is the force applied to the beam end, L is the length of the beam, x is the position along the beam, E_b and E_f are the Young's modulus of the beam material and the film material, and t_b is the thickness of the beam. The values of material properties and dimensions are summarized in Table 3. Since the thickness of the beam is much greater than the thin film, the above equation can be rewritten as

$$\varepsilon_{xf} = \frac{6F(L-x)}{E_b w t_b^2} \tag{2.6}$$

Table 3: Material properties and dimensions [63].

E_b	185 GPa (Si)
E_f	245 GPa (NiCr 80-20 wt.%)
v_b	0.278 (Si)
v_f	0.325 (NiCr 80-20 wt.%)
t_b	15 μm
t_f	0.1 μm
w	980 μm
L	400 μm

Note that when quantifying the sensor response, the strain will be simulated instead of calculated using the above equations.

Let the Poisson's ratio of the beam material be v_b and the Poisson's ratio of the film material be v_f. The transverse strain and the vertical strain for a free film can be expressed using the axial strain based on the Poisson's effect.

$$\frac{dL_f}{L_f} = -\frac{1}{v_f}\frac{dw}{w} = -\frac{1}{v_f}\frac{dt_f}{t_f} \tag{2.7}$$

Considering that $t_f << t_b$ and the sensor is attached to the beam, the axial and transverse strain of the film should be the same with the beam unless the sensor is detached from the beam. We have

$$\varepsilon_{xf} = \varepsilon_{xb} \tag{2.8}$$

$$\varepsilon_{yf} = \varepsilon_{yb} \tag{2.9}$$

ε_x and ε_y will be used for simplicity. In the transverse direction, the film is 'dragged/compressed' more comparing to the free film (unattached to a beam). This 'dragging/compressing' effect affects the vertical strain, ε_z, by introducing a $-v_f(v_f - v_b)\varepsilon_x$ term, where $-(v_f - v_b)\varepsilon_x$ is the additional transverse strain due to the beam. From Eqn. 2.7, the transverse and vertical strain of the sensor can be calculated by the following equations

$$\varepsilon_y = -v_b \varepsilon_x \tag{2.10}$$

$$\varepsilon_z = -v_f \varepsilon_x + v_f(v_f - v_b)\varepsilon_x \tag{2.11}$$

The fractional change in resistance can be expressed in terms of the axial strain and the change in resistivity

$$\frac{\Delta R}{R} = \frac{\Delta \rho}{\rho} + (1 + v_b + v_f - v_f(v_f - v_b))\varepsilon_x \tag{2.12}$$

For the simplicity, define K as

$$K = 1 + v_b + v_f - v_f(v_f - v_b) \tag{2.13}$$

Define R_{xy} as the resistance of an element with length dx and width dy. There are $(x_1 - x_2)/dx$ elements in a row and $(y_1 - y_2)/dy$ rows in the sensor. R_{xy} can be expressed as

$$R_{xy} = (\frac{dx}{x_1 - x_2}\frac{y_1 - y_2}{dy})R \tag{2.14}$$

Replacing $1 + v_b + v_f - v_f(v_f - v_b)$ in Eqn. 2.12 with Eqn. 2.13, the fractional change in resistance of this element can be written as

$$\frac{dR_{xy}}{R_{xy}} = \frac{d\rho}{\rho} - K\frac{dx}{x} \tag{2.15}$$

Integrating from x_1 to x_2, we have the absolute change in resistance of all the elements at position y (one row of elements), $\Delta R_y(y)$

$$\Delta R_y(y) = \int_{x_1}^{x_2} dR_{xy} = \int_{x_1}^{x_2} (\frac{d\rho}{\rho} - K\varepsilon_a(x, y))R_{xy}dx \tag{2.16}$$

$\varepsilon_a(x, y)$ denotes the strain at position (x,y). Considering the number of elements in the simulation are limited, we use sum instead of integration when calculating the resistance change in one row, Δx and Δy denote the length and width of each element

$$\Delta R_y = \sum_{x_1}^{x_2} \Delta R_{xy} = \sum_{x_1}^{x_2} (\frac{d\rho}{\rho} - K\varepsilon_{axy}) R_{xy} \Delta x \tag{2.17}$$

The stress-free resistance of all elements in one row is

$$R_y = (\frac{y_1 - y_2}{\Delta y}) R \tag{2.18}$$

The total resistance of the sensor under stress is the parallel combination of resistance of each row (stress-free resistance + change in resistance)

$$R' = \frac{1}{\frac{1}{R_y + \Delta R_{y1}} + \frac{1}{R_y + \Delta R_{y2}} + \cdots + \frac{1}{R_y + \Delta R_{yn}}} \tag{2.19}$$

The total change in resistance of the strain sensor is

$$\Delta R = R' - R \tag{2.20}$$

Using the above algorithm we calculate the resistance change of the sensor based on the simulated strain corresponding to a certain contact force.

2.3.4 Optimization for Maximum Force and Angle Resolution

To ensure maximum force and angle sensitivity, the strain sensors need to be optimized in terms of size and location. When the probe is contacting the test substrate with angular misalignment, the strain is larger on the side that makes the contact first. The classical cantilever model which describes the behavior of a beam with one end fixed under a point load can be used in this analysis [48]. This point load (contact force) at the probe tip introduces a torque, T, which twists the probe chip until all three tips contact the substrate, as shown in Figure 2.16. The contact force, F, can be equated to a torsional loading and two loading forces, as shown in Figure 2.17. The torsional loading can be calculated by,

$$T = 2(\frac{F}{2})x = Fx \tag{2.21}$$

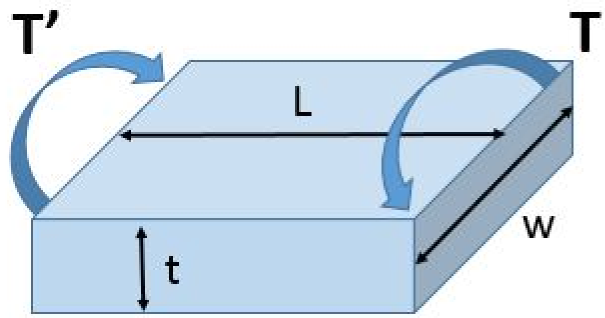

Figure 2.16: Model of a beam under a torsional loading.

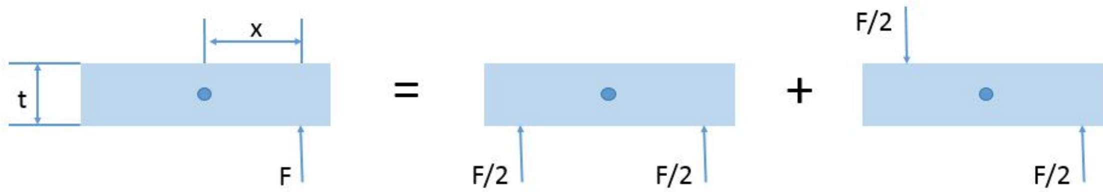

Figure 2.17: Cross-section view of a beam under a point loading and its equalized loadings.

To over come a 1° tilt, the required force can be calculated by the torque required to create a 1° tilt, the force required to create such torque, and the spring constant of the beam, k,

$$\theta = \frac{TL}{cwt^3G} \tag{2.22}$$

$$k = \frac{1}{4}Ew(\frac{t}{L})^3 \tag{2.23}$$

where G is the shear modulus of elasticity (52 GPa for Si), E is the elastic modulus (185 GPa for Si) and L, w, t are the dimensions of the beam, as shown in Figure 2.16. The coefficient c for w/t greater than 5 can be expressed as [50]:

$$c = \frac{1}{3}(1 - 0.63\frac{t}{w}) \tag{2.24}$$

Please note that all the above analysis is based on a simplified model. The maximum shear stress occurs along the centerlines of the wider face of the beam. However, due to the design of the probe chip, the strain distribution is quite different from a simple beam. To predict the probe behavior, the actual mechanical performance of the probe (strain distribution, spring constant, etc.) needs to be simulated using ANSYS.

To measure the angle of misalignment most effectively, the strain sensors should be placed symmetrically at positions with the biggest difference in strain when the probe is tilted. To measure the contact force effectively, the sensors need to be placed at positions where the strain is as high as possible when the probe is in contact. For the example shown in Figure 2.18, the angular sensitivity is the major factor to consider during the sensor optimization process due to the fact that even with a relatively large tilt (0.3°), the difference in strain between selected locations is small compared to the absolute value.

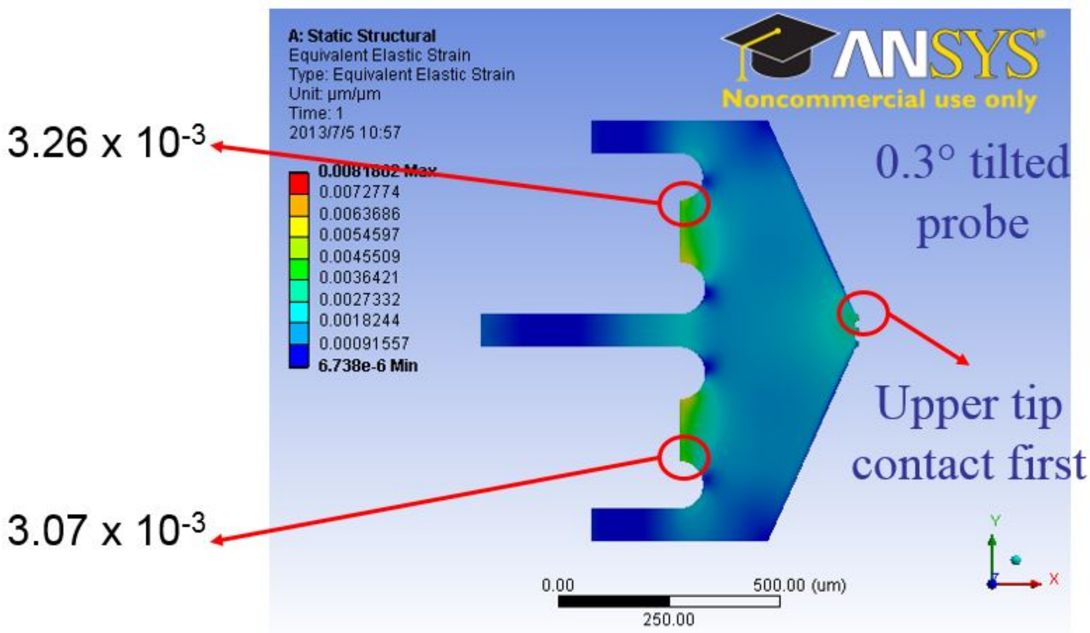

Figure 2.18: Simulated strain distribution profile of WR-1.5 probe with 0.3° angular misalignment – upper tip contacting test substrate first, 20 mN contact force.

Figure 2.19 shows the optimization flow of the strain sensor. First, the simulated strain distribution profile is replotted in Matlab. The simulation was done using the finite element method (FEM) in ANSYS. Hence, each element is a tetrahedron. For the convenience of calculation, the probe is remeshed into cubicles in Matlab. The strain in each cubicle is decided by the average stain of adjacent tetrahedra. The sensor is placed on the top surface of the probe to simplify the electrical connection and probe assembly process. So only the top elements of the probe are selected which compose a probe ‘sheet’ in the x-y plane (thickness of the elements can be ignored) indicated in Figure 2.19.

The strain differences at symmetrical positions on the probe are taken, which is equivalent to ‘folding’ the top half down about the red dotted line in Figure 2.19 and taking the difference between the two halves. From the result shown in Figure 2.19, two areas have higher values in strain difference. To ensure that the sensors do not interfere with the probe’s

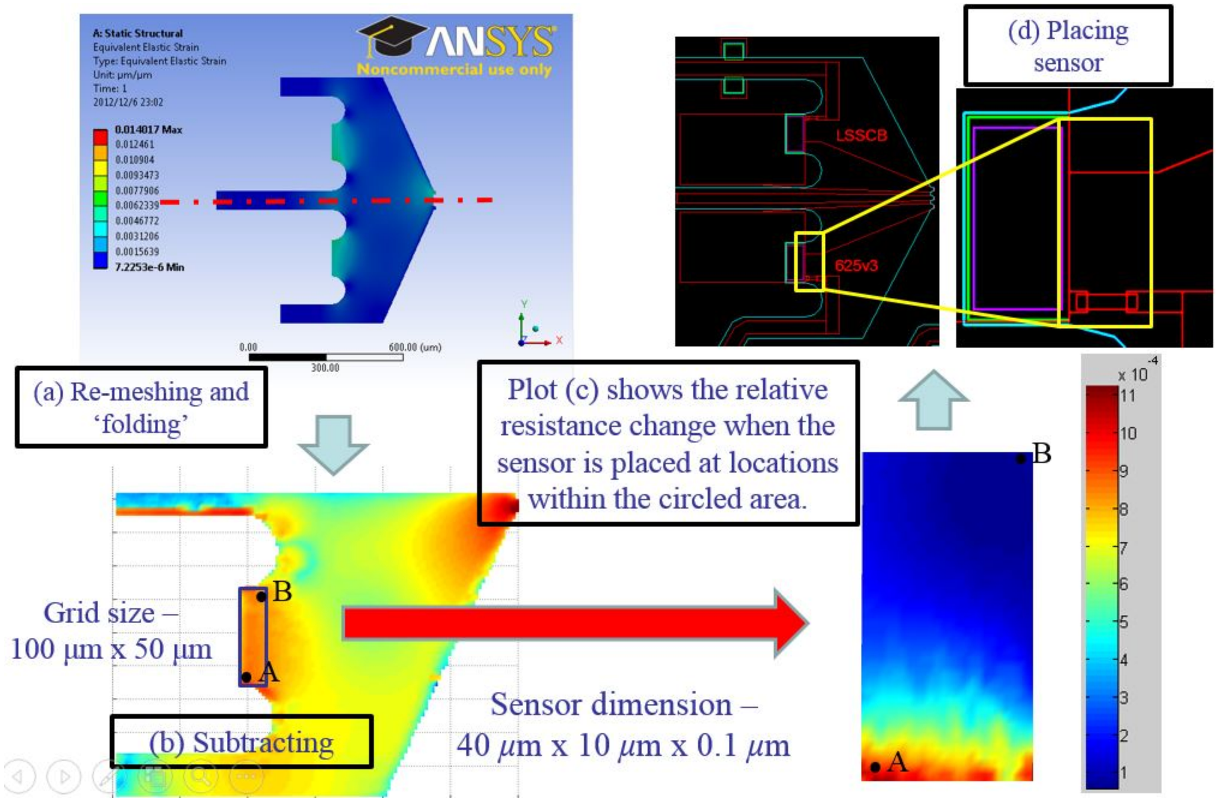

Figure 2.19: Optimization flow of the sensor. Plot (c) shows the relative resistance change when the sensor is placed at locations within the circled area - point A has the highest relative resistance change when the probe is making a tilted contact, i.e., the optimum location for the sensor; point B has the lowest relative resistance change, i.e., lowest sensitivity for the sensor.

RF performance, the area close to the clamp region is selected for further optimization.

The next step is to determine the sensor size and exact location. An algorithm is developed to find the optimum location. For a given sensor size, the sensor response at all locations within the selected area is calculated using the algorithms described in Section 2.3.3. The Poisson's ratio of the beam material (Si) and sensor material (NiCr) used in the calculation are 0.278 and 0.325. As shown in Figure 2.19(c), the strain differences are higher near the lower edge (within approximately 15 μm). To ensure the maximum sensitivity, the sensor should only cover areas with high strain differences. Considering the fabrication accuracy, 10 μm is used for the sensor width. Sensor lengths between 30 μm and 80 μm are simulated. The relative change (ΔR/R) in resistance for sensors with different lengths are plotted in Figure 2.20.

After a few iterations, the final results indicate that the sensor lengths should be 40 μm and the lower left corner of the sensor should be placed 15 μm above the lower edge and

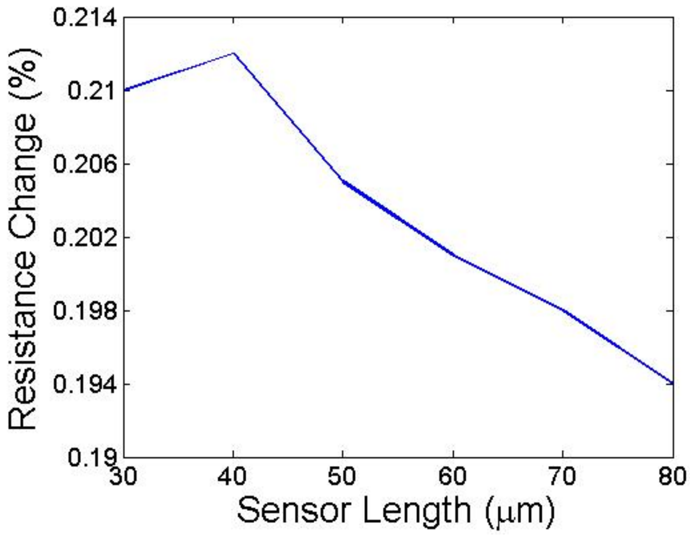

Figure 2.20: Relative change in resistance for sensors with different lengths.

5 μm right to the left edge of the selected area (as shown in Figure 2.19(d)). Based on results shown in Figure 2.12, this location is not optimal for contact force sensing, but has sufficiently large strain and will not compromise the contact force sensitivity much.

With no angular misalignment and 20 mN contact force, the probe deflection should be 21.7 μm and the average strain, ε, that is measured by the sensor is 1.9×10^{-3}. The NiCr thickness for the strain sensor is chosen to be 0.1 μm. The TCR of thinner NiCr films increase significantly [58] (23 to 57 ppm/°C [64]) while a thicker film has a lower sheet resistance that would effectively decrease the sensitivity due to the wiring. After optimization, the final dimensions of the strain sensor are 40 μm $\times$ 10 μm $\times$ 0.1 μm. Figure 2.21 shows an SEM image of the fabricated probe. A measure of how sensitive the NiCr resistor is to the mechanical strain, gauge factor (GF), is defined to calculate the change in resistance using the average strain.

$$GF = \frac{\frac{\Delta R}{R}}{\varepsilon} \tag{2.25}$$

The gauge factor of 0.1 μm thick NiCr 80/20 wt.% film is 1.4 [64]. The resistance, R, of each sensor should be 60 Ω (the resistivity of NiCr 80/20 wt.% at room temperature is 1.5×10^{-6} $\Omega\cdot$m) [65]. Using Eqn. 2.25, the resistance of each sensor will increase by 160 mΩ. With 0.3° angular misalignment and 20 mN contact force, the difference between the strain sensors will be 15.9 mΩ.

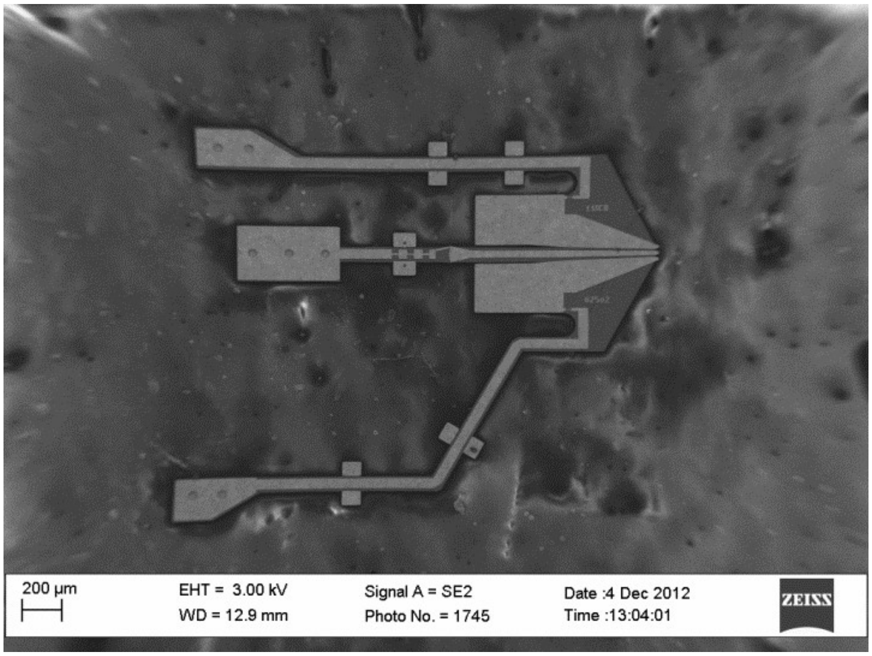

Figure 2.21: An SEM image of the fabricated probe.

2.3.5 Mechanical Test

The mechanical measurements are conducted similarly as in the work of Chen et al. on an automated probe positioning stage [44]. A load cell (Futek FSH0234) is used to measure the contact force generated by the probe contact (shown in Figure 2.22). A goniometer stage (Newport 481-A) is mounted on the motor-drive stage to change the contact angle by tilting the test substrate.

The purpose of sensor performance evaluation is to ensure that the integrated strain sensors provide repeatable response to a certain contact force as well as measuring the probe contact angle accurately and precisely. The measured resistance of the sensors are 57.54 Ω (R1) and 56.60 Ω (R2). To evaluate the angular misalignment more accurately, each sensor is measured in a Wheatstone-bridge circuit (shown in Figure 2.23) built external to the waveguide block. The sensor is connected as R_D in Figure 2.23. The output of the bridge circuit is calculated in Eqn. 2.26.

$$V = (\frac{R_D}{R_C + R_D} - \frac{R_B}{R_A + R_B})Vs \tag{2.26}$$

V_S of 1 V is used. Resistors R_A, R_B, and R_C are matched to R1 and R2 within 1%. The output of each bridge circuit is amplified by a low noise instrumentation amplifier (Texas

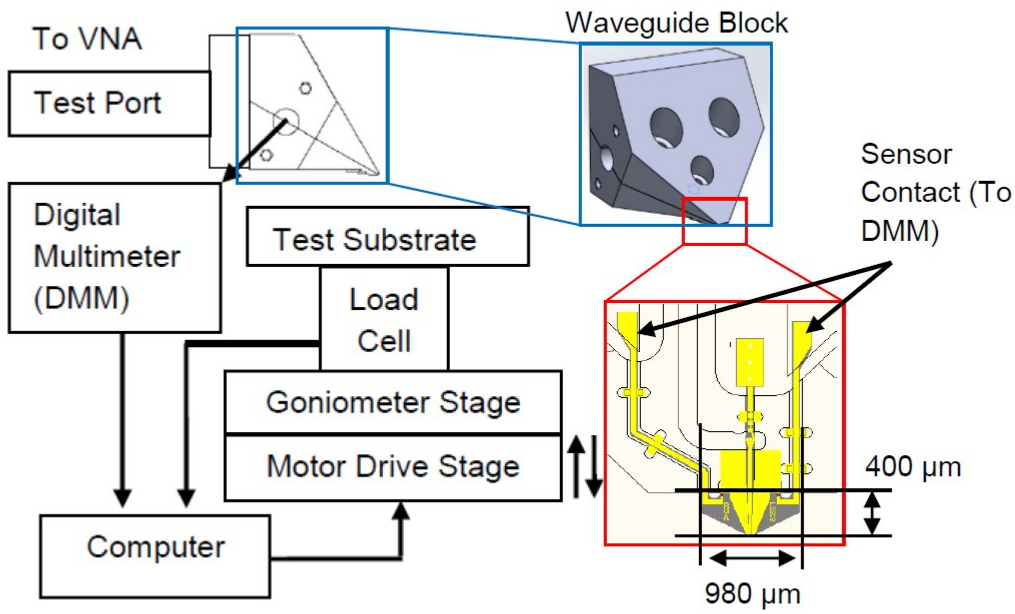

Figure 2.22: Micromachined terahertz probe (with integrated strain sensor) test setup.

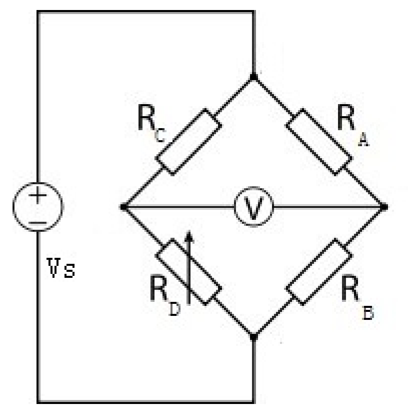

Figure 2.23: Wheatstone-bridge circuit.

Instruments INA103, 1 nV/$\sqrt{Hz}$ input voltage noise) with a voltage gain of 100 to increase measurement resolution and improve signal-to-noise ratio [66]. The motor controlled stage with load cell mounted on top is moved up by 2 μm steps until a 13 mN contact force is reached (measured by the load cell). During this process, the strain of the resistive sensor is increasing due to the probe deflection, thus the resistance should increase accordingly which results in increased output of the bridge circuit. Figures 2.24a and 2.24b show the measured output of the sensor pair for a probe with 0.35° angular misalignment during one contact cycle (contact force increases by approximately 1 mN step from 0 mN to 13 mN, measured by the load cell). The output voltage from the amplifier is measured by a Keithley 2000 Digital Multimeter and averaged from 10 independent measurements. The response of the sensor on the side with larger strain (ΔV1) is 90.1 mV, whereas the response of the sensor on the opposite side (ΔV2) is 82.4 mV. With increased or decreased angular misalignment, the difference between the outputs of the two bridge circuits (ΔV1 – ΔV2) increases or decreases accordingly. Figure 2.25 shows both simulated and measured results of the difference between the two bridge circuit responses vs. angular misalignment with standard deviation error bars calculated from 10 independent measurements. For angular misalignment about the center, 0.05° rotation is associated with 1.99 $\pm$ 0.4 mV voltage variation. For contact angle within $\pm$0.35°, the measurement accuracy is $\pm$0.025°. For angular misalignment greater than 1.3°, the sensor pair tends to saturate due to the probe contact mechanism, i.e., the difference between the strains of the two sides is saturated.

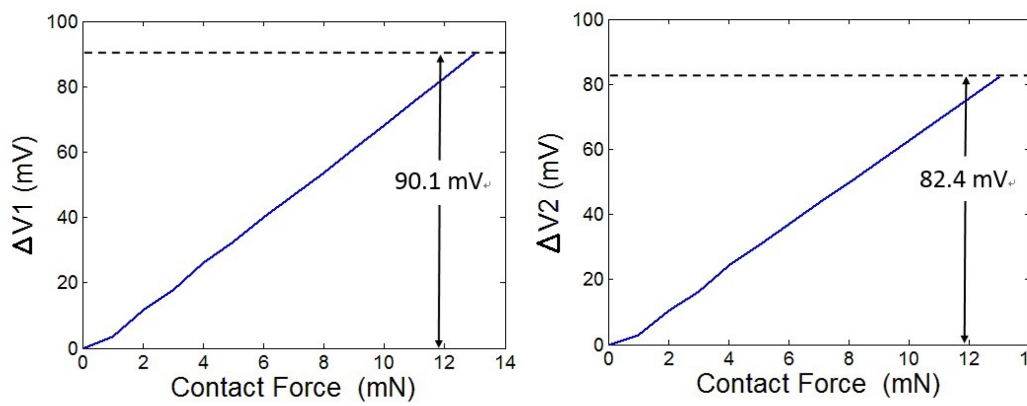

(a) (b)

Figure 2.24: Average bridge circuit outputs of strain sensor on a probe with 0.35° angular misalignment vs. contact force measured by load cell from 10 independent contacts.

According to the results shown in Figure 2.25, the angular misalignment can be compensated based on the difference between the responses of the two sensors. As shown in Figure 2.26, when angularly aligned, the measured outputs of the two sensors vs. contact force agree well with each other. With 13.5 μm probe deflection at 13 mN, the measured outputs of the bridge circuits increase by 86.1 mV (R1) and 87.5 mV (R2), as compared to a simulated value of 86.7 mV with 14.1 μm probe deflection at 13 mN. The measured spring constant of the probe is 0.96 $\pm$ 0.03 mN/μm, which agrees with the simulated value (0.92 mN/μm). In addition, when angularly aligned (ΔV1 = ΔV2), 1 mN contact force step corresponds to 6.6 $\pm$ 0.5 mV voltage variation, which indicates an approximate contact force resolution of 0.2 mN. The recorded temperature variation during all mechanical measurements is within $\pm$0.21°C. Due to the low TCR of the NiCr film, temperature variation

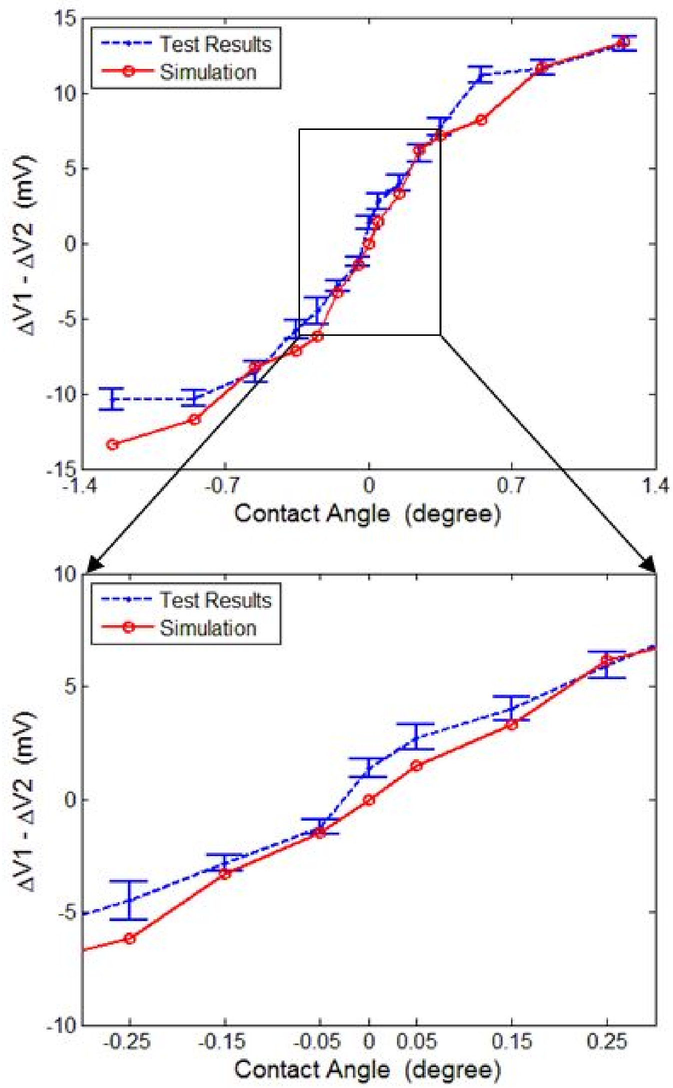

Figure 2.25: Difference between two bridge circuit responses vs. angular misalignment (contact angle) with error bars from 10 independent contacts.

within ±0.4°C will not affect the measurement uncertainty. Temperature variation beyond ±0.4°C can be compensated accordingly.

Each probe will be calibrated mechanically before the RF measurements to address the variation due to fabrication tolerances and ensure accuracy. Mechanical tests show that the integrated sensors have a contact force resolution of 0.2 mN and a contact angle resolution of 0.05° about the center. Taking advantage of the strain sensor, the RF measurement repeatability can be improved by accurate force control. Also, probe lifetime can be extended by planarizing the probe with the test substrate to reduce contact force.

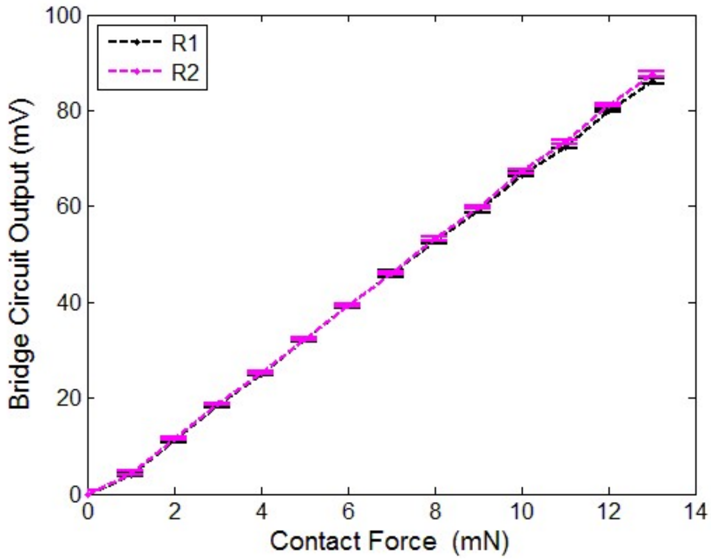

Figure 2.26: Average response of strain sensor on an angularly aligned probe vs. contact force measured by load cell from 10 independent contacts.

2.3.6 RF Test

The RF measurements are conducted similarly to the recently published work of Chen et al. [44]. A two-tier calibration technique is used to obtain the S-parameters of the probe [43]. Scattering parameter (S-parameter) measurements are taken with a one-port WR-1.5 frequency extension unit from Virginia Diodes Inc. (VDI WR1.5 VNAXTXRX) and a Rohde & Schwarz ZVA-40 network analyzer. The initial calibration is done to a reference plane coincident with the frequency extension unit waveguide test port, using a short, quarter-wave delayed short, a radiating open [67] and a precision load. The second tier is done with the probe attached to the test port and performed by terminating the CPW probe with on-wafer calibration standards: a CPW short and four CPW delayed shorts of different lengths [44]. The CPW short-end is inductive due to the current distribution in the discontinuity region [68], [69]. In this work, the calibration standards, short and delay shorts, are modeled using HFSS, as done by L. Chen *et al.* [44]. The CPW dimensions are 4/7/4 μm for widths of the gap and the center conductor with other dimensions detailed in Figure 2.27. The electrical lengths of the delayed shorts are evenly distributed from 0° to 180° at 625 GHz, excluding the 180°. The S-parameters of the probe assembly are extracted using the error networks produced by both calibrations [43], [44].

The WR-1.5 probe with integrated strain sensor is measured repeatedly at 11 mN contact

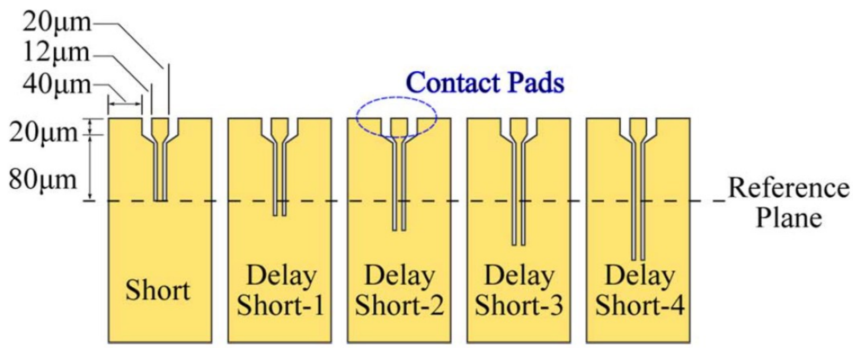

Figure 2.27: Dimensions of CPW calibration standards [44].

force using the same set of calibration standards. Prior to making a probe contact, a rough angular alignment is performed using a standard bubble level. Firstly, the contact force is controlled by the strain sensor. From Figure 2.26, at 11 mN, the associated strain sensor response is approximately 73 mV. Thus, during the 2nd tier calibration, the stage is stopped when 73 mV (11 mN) is reached and data are taken for each CPW standard. An average of 10 independent measurements, i.e., probe calibrations, of the probe with 11 mN contact force controlled by the strain sensor is shown in Figure 2.28. The measurement results match simulation shown in Figure 2.14. Machining tolerances, waveguide losses, and misalignment of probe chip can cause the measured data to deviate from simulation. The magnitude of S_{21} drops around 550 GHz due to the electromagnetic absorption by water [70].

The next experiment is to control the 11 mN contact force using the load cell. The actual contact force measured by the load cell is 11 ± 1.3 mN. The average magnitudes of S_{21} with error bars indicating complex standard deviation [71] from 10 independent measurements controlled by the load cell are shown in Figure 2.29. As a comparison, the result of 11 mN probe contact controlled by the strain sensor is also included in Figure 2.29. The maximum complex standard deviation of S_{21} controlled by the load cell is 0.119 dB across the band (same for S_{12}) as compared to the 0.125 dB maximum complex standard deviation of S_{21} controlled by the strain sensor.

Based on the measurement results shown above, the use of a load cell for on-wafer probing can be replaced with an integrated strain sensor. It not only provides comparable measurement repeatability, but also enables accurate contact force measurement without modifying the probe station. This method is especially beneficial for probing large wafers where the wafer thickness profile may vary by 5 to 10 μm. Such variation can lead to 3 to

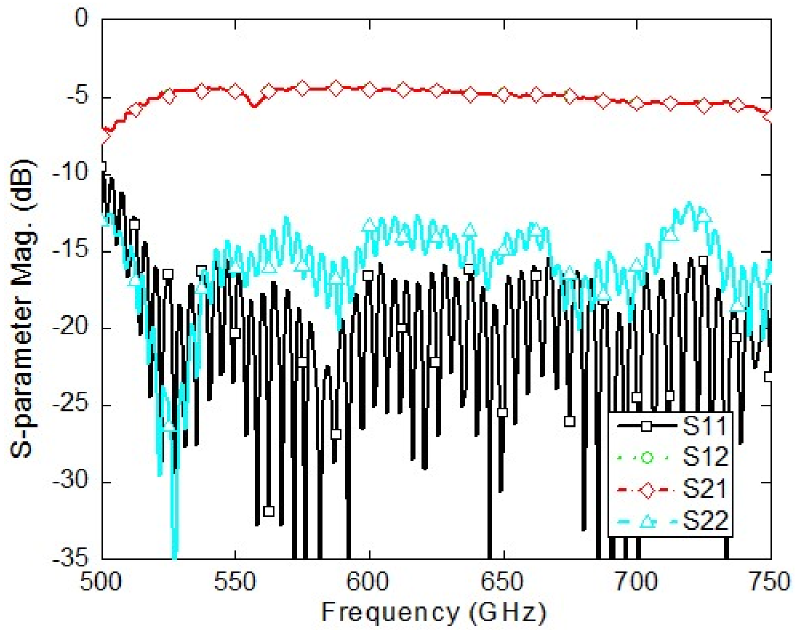

Figure 2.28: Average magnitude of S-parameters of WR-1.5 probe from 10 independent measurements (contact force measured and controlled by strain sensor).

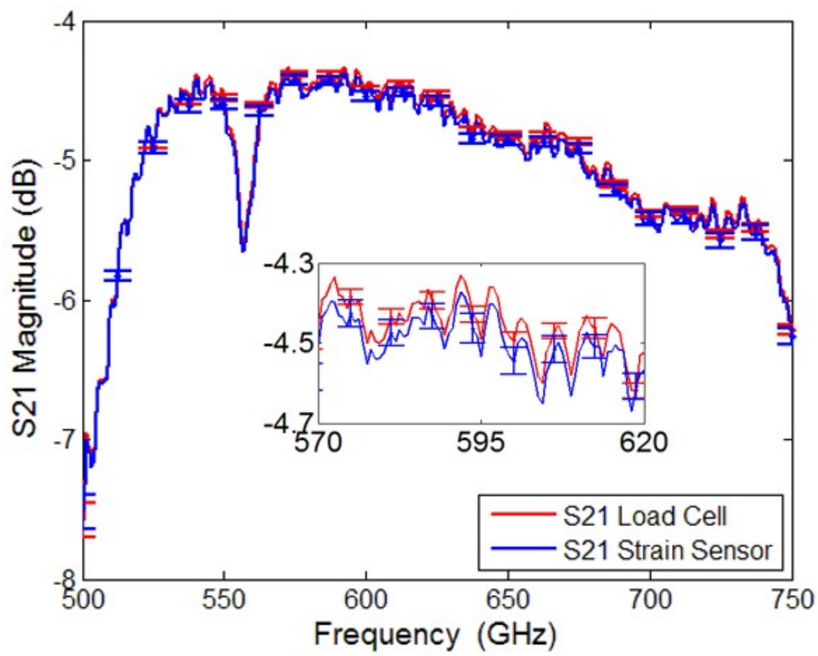

Figure 2.29: Average S_{21} magnitudes of WR-1.5 probe from 10 independent measurements (contact force measured and controlled by both strain sensor and load cell).

6 mN variation in contact force for a probe with 0.65 mN/μm spring constant (probe with no integrated strain sensor) [44].

As shown previously, strain sensors positioned symmetrically on the probe can detect

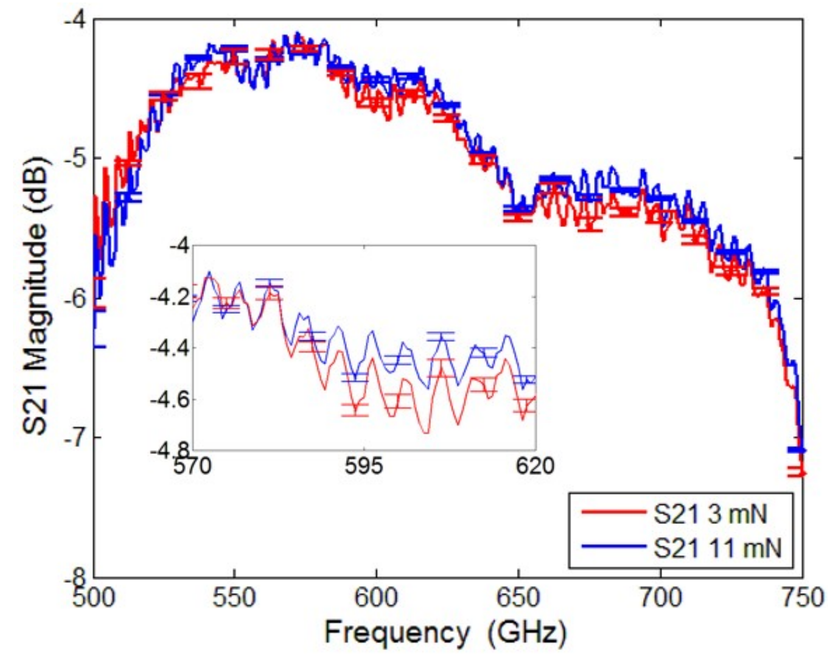

Figure 2.30: Average S_{21} magnitudes of WR-1.5 probe from 10 independent measurements with 3 mN contact force (aligned by strain sensor) and 11 mN contact force (aligned by bubble level).

contact angle by sensing asymmetrical strain generated during contact if the probe is angularly misaligned. Such angular misalignment can be compensated by tilting the test substrate or the probe accordingly. For a contact angle close to 0°, the required contact force to form low resistance contacts for all tips is reduced to 3 mN [43]. Using the integrated strain sensors, the probe is angularly aligned to the test substrate within ±0.025° at first. Then 10 independent measurements are taken with 3 mN contact force controlled by the load cell. Figure 2.30 shows the average magnitudes of S_{21} with error bars indicating complex standard deviation for 3 mN probe contact aligned by the strain sensors. As a comparison, the result of 11 mN probe contact aligned by the bubble level is also included in Figure 2.30 (same set of calibration standards as 3 mN). Note that the measurements shown in Figure 2.29 and Figure 2.30 are performed using different probes at different times. The shift in S_{21} at the band edges is due to the alignment tolerance of the probe chip to the metal block, whereas the ambient humidity variation explains the discrepancy around 550 GHz. The maximum complex standard deviation of S_{21} using 3 mN contact force is 0.104 dB across the band (same for S_{12}) as compared to the 0.132 dB maximum complex standard deviation of S_{21} using 11 mN contact force.

The following study demonstrates how the contact force and angular alignment affect the measurement repeatability. The relative standard deviation (%RSD, defined in Eqn. 2.27) of S-parameters (S_{21}) is used to quantify the measurement repeatability.

$$\%RSD = \frac{complex\ standard\ deviation}{mean} \times 100\% \tag{2.27}$$

10 independent measurements at 0°, 0.15°, 0.25°, and 0.35° contact angle, each with ±0.025° accuracy, are taken with 11 mN contact force measured by the load cell. Another set of 10 independent measurements are taken with 3, 5, 8, and 11 mN contact force measured by the load cell at 0° and 0.15° with ±0.025° accuracy using the same set of calibration standards. For a constant contact force of 11 mN, the relative standard deviation of S_{21} reduces with contact angle (Figure 2.31a). When the contact angle is below 0.15°, the relative standard deviation of S_{21} stabilizes around 0.5% for frequencies above 550 GHz. For a constant contact angle of 0.15°, the relative standard deviation of S_{21} decreases when contact force increases (Figure 2.31b). For contact forces above 5 mN, the relative standard deviation of S_{21} stabilizes below 1% for frequencies above 550 GHz. For a constant contact angle of 0°, the relative standard deviation of S_{21} stabilizes below 0.5% for frequencies above 550 GHz when the contact force is greater than 3 mN (Figure 2.31c). This phenomenon agrees with previous experimental results that a contact force of 1 mN per tip is required to obtain a low contact resistance [43].

According to the results indicated in Figure 2.30, 2.31a-2.31c, by aligning the micro-machined probe to the test substrate, repeatable RF measurements can be achieved with significantly lower contact force (< 5 mN) compared to a previously reported value of 15 mN [72]. Consequently, extended probe lifetime is expected due to the lower impact on the probe tips without overdriving during the probe contact and even mechanical wear on each tip.

Table 4: Phase Error of Delay Short-2 @ 625 GHz.

	625 GHz
Contact Force Controlled by Strain Sensor (11 mN)	0.56°
Variable Contact Force (3 – 11 mN)	5.25°

To further substantiate the improvement in measurement accuracy provided by the strain sensor, one of the delay shorts (Delay Short-2 shown in Figure 2.27) is measured

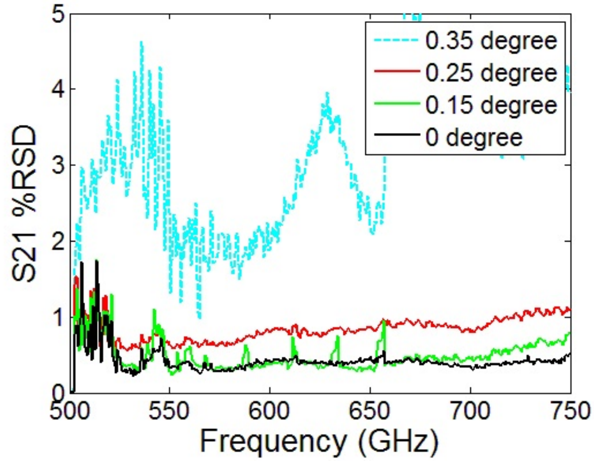

(a)

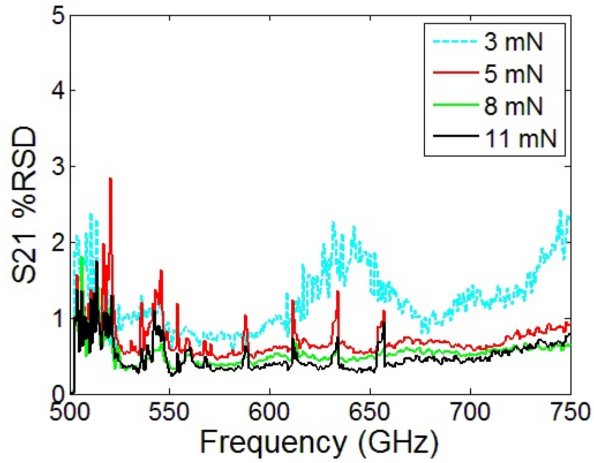

(b)

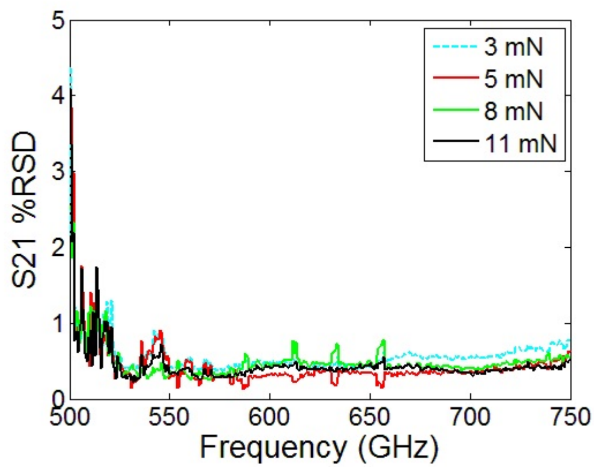

(c)

Figure 2.31: Relative standard deviation of S-parameters vs. frequency from 10 independent measurements: (a) 11 mN contact force; (b) 0.15° contact angle; (c) 0° contact angle.

using the WR-1.5 probe with integrated strain sensor in two experiments. First, the probe is calibrated with the contact force controlled at 11 mN by the strain sensor. 12 independent measurements of Delay Short-2 are taken using the same contact force. Second, the same measurements are repeated 3 times using 3, 5, 8, and 11 mN contact force each. The phase errors at midband (625 GHz) are shown in Table 4. The measurement repeatability is significantly improved for the measurements with a stable contact force. For probes without a strain sensor, the contact force may vary by 6 mN or even more depending on the wafer thickness profile of the test wafer. This contact force variation will result in positioning error of the probe tip, which is the dominant factor in measurement uncertainty [44].

2.4 Summary

This chapter presents an improved method for monitoring and controlling the contact condition of terahertz on-wafer probes which improves the repeatability of terahertz probing and enables accurate contact force measurement without modification to the standard probe station. Repeatable RF measurements are achieved by controlling the contact force and contact angle using the integrated strain sensors. By properly sensing and controlling the planarity of the terahertz probes, the required contact force can be significantly reduced to extend probe lifetime. Mechanical tests show that the integrated sensors have a contact force resolution of 0.2 mN and a contact angle resolution of 0.05° about the center. RF tests show that repeatable measurements can be achieved with 3 mN contact force after adjusting the probe contact angle within ±0.025° using the integrated sensors. For contact angle within ±0.15°, 5 mN contact force is sufficient to achieve repeatable measurements. In addition, measurement repeatability is also improved by angularly aligning the probe tips (reducing contact angle).

3 Large Wafer Measurement Uncertainty Characterization

3.1 Introduction

This Chapter introduces a complete measurement uncertainty characterization of one-port large wafer probing in the WR-1.5 (WM-380: 500-750 GHz) band. Factors that contribute to measurement uncertainty, including contact force variation, stage accuracy and repeatability, and source uncertainty are discussed. Experiments are designed to characterize and analyze each factor. A micromachined WR-1.5 probe with integrated strain sensor is used to measure calibration standard sets at different locations on a 2-inch wafer. Measurement results of the strain sensor assisted WR-1.5 probe are presented. In addition, recommended probe station specifications and procedure for terahertz probing without an integrated strain sensor are developed.

To ensure the accuracy of on-wafer measurement results, measurement uncertainty must be characterized precisely. At microwave frequencies, on-wafer measurement uncertainty estimation is a subject of long-standing interest [73–75]. Generally, three major factors contribute to the measurement uncertainty, including source uncertainty, contact force variation, and stage accuracy and repeatability. However, due to the relatively long wavelengths, the effects of wafer thickness variation across a large wafer and stage accuracy and repeatability on on-wafer probing at microwave frequencies have not drawn much attention. At submillimeter-wave frequencies, these issues lead to significant phase error and need to be addressed [44].

In this work, the measurement uncertainty is characterized on a 2-inch wafer (shown in Figure 3.1) using a micromachined WR-1.5 probe with a pair of NiCr (80-20 wt.%) integrated strain sensors described in Chapter 2. The integrated sensors eliminate the need for observing scratch marks on test pads to determine the probe contact condition. They enable accurate measurements of both probe contact force and angular alignment, which are crucial for RF measurement repeatability. Probe contact force is monitored in situ by measuring strain generated by vertical deformation. Angular misalignment can be detected by sensing asymmetrical strain on symmetrical positions of the probe. By properly monitoring and controlling the probe contact using the integrated strain sensors, enhanced measurement accuracy and repeatability, as well as extended probe lifetime, can be achieved. In addition, this method requires no modification to the standard probe station. Figure 3.2 shows the test setup of the micromachined THz probe with integrated strain sensor for large wafer measurement. In this section, the integrated strain sensor is used as a tool to evaluate the measurement uncertainty. Recommended probe station specifications and procedures for standard terahertz probing without the use of the integrated strain sensor are also developed based upon the results of this section.

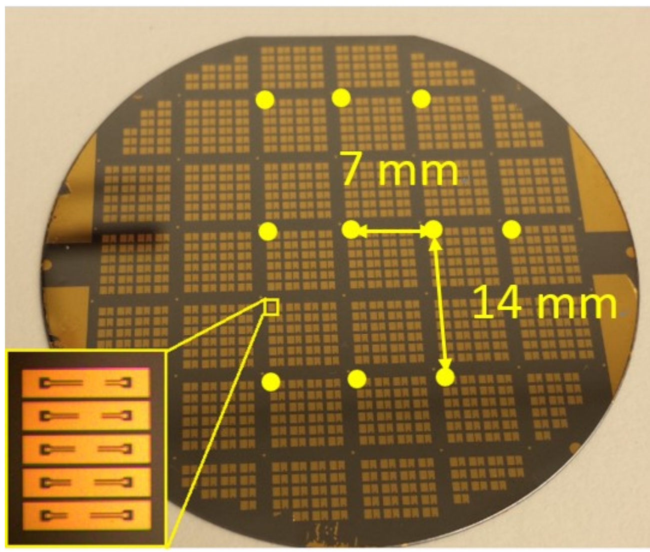

Figure 3.1: The positions (marked) of the measured sets of calibration standards on the 2–inch wafer.

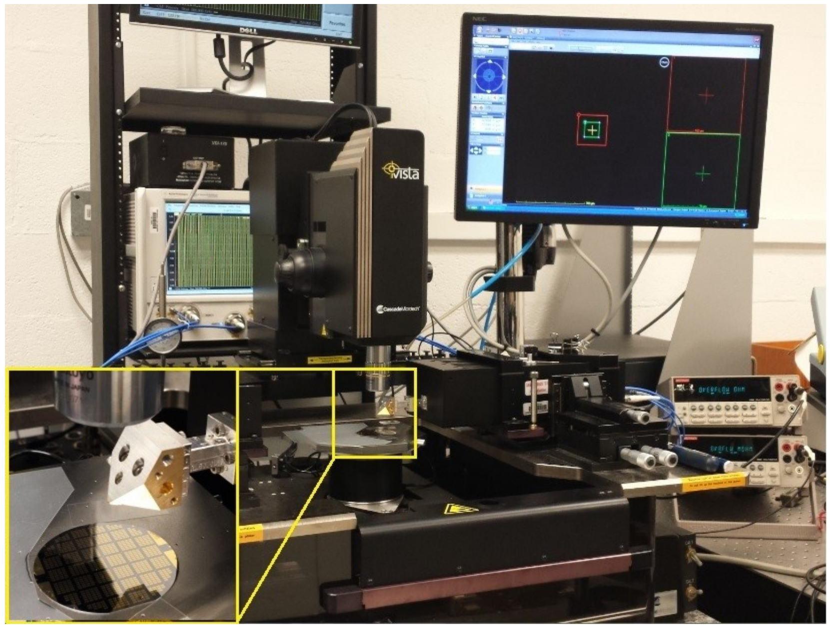

Figure 3.2: Test setup of micromachined terahertz probe (with integrated strain sensor) for large wafer measurement.

3.2 Experiments and Results

There are three major factors that contribute to the measurement uncertainty, including contact force variation, stage accuracy and repeatability, and source uncertainty. In order to characterize the effect of each factor on the measurement uncertainty, a few experiments are designed to minimize the effects of other factors. As in Section 2.3.6, the relative standard deviation (%RSD) of S-parameters (S_{21}) of the probe assembly is used as a quantitative measure of repeatability. The same two-tier calibration technique is used to determine the S-parameters of the probe assembly (see Section 2.2.2). S-parameter measurements are taken using a one-port WR-1.5 frequency extension unit from Virginia Diodes Inc. (VDI WR1.5 VNAXTXRX, 7 dBm RF, 10 dBm LO, 18th harmonic factor) with a micromachined waveguide twist [76], an Agilent PNA-X N5245A vector network analyzer (1 kHz IF bandwidth, 401 points) and a Cascade Microtech PA200 probe station. For all experiments presented in this chapter, the probe assembly is warmed up on the test port for a minimum of 20 minutes prior to recording data due to the temperature difference between an operating VNA extension module and room temperature. A simple experiment can validate the 20 minutes wait time. After calibrating the VNA extension module (using a short, a quarter-wave delayed short, a radiating open [67] and a precision load), a short is connected to the test port and measured every minute. Figure 3.3 shows the phase standard deviation of S_{11} of the short in different time periods. The phase standard deviation of S_{11} stabilizes after 20 minutes, which means the system is stabilized (warmed up). After warming up the probe assembly, the system drift does not perturb the results since all measurements are performed close in time (within 30 minutes). As shown in Figure 3.3, the phase standard deviation of S_{11} does not vary significantly in a 30 minute period.

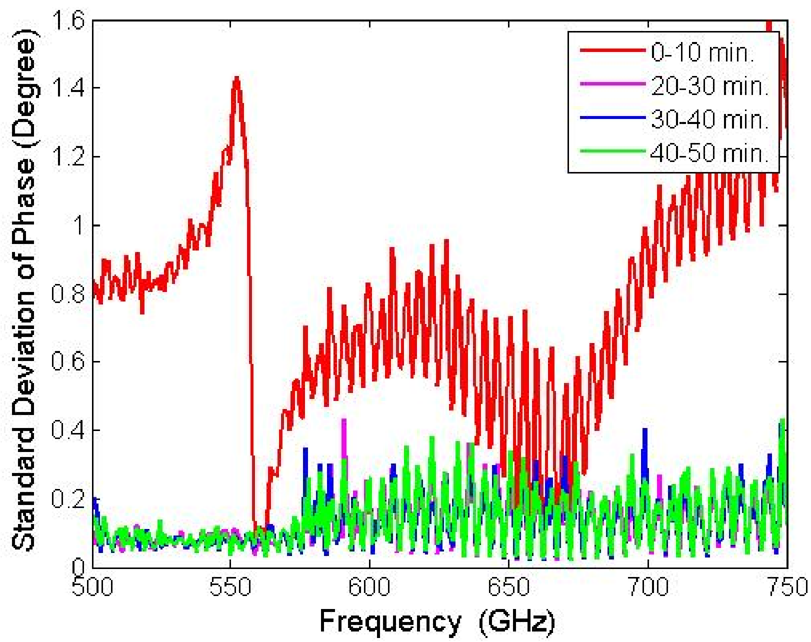

Figure 3.3: Phase standard deviation of a short connected to the test port of the frequency extension unit.

The initial rectangular waveguide calibration is done to a reference plane coincident with the frequency extension unit test port, using a short, a quarter-wave delayed short, a radiating open [67] and a precision load. The second tier calibration is done with the probe attached to the test port and performed by terminating the CPW probe with on-wafer calibration standards: a CPW short and four CPW delayed shorts of electrical lengths evenly distributed from 0° to 180° at 625 GHz, excluding the 180° [44]. The CPW dimensions are 4/7/4 μm for widths of the gap and the center conductor with other dimensions detailed in Figure 3.4. The S-parameters of the probe are extracted using the error networks produced by both calibrations [43], [44]. The average magnitude of S-parameters of a WR-1.5 probe from 10 independent measurements are shown in Figure 3.5.

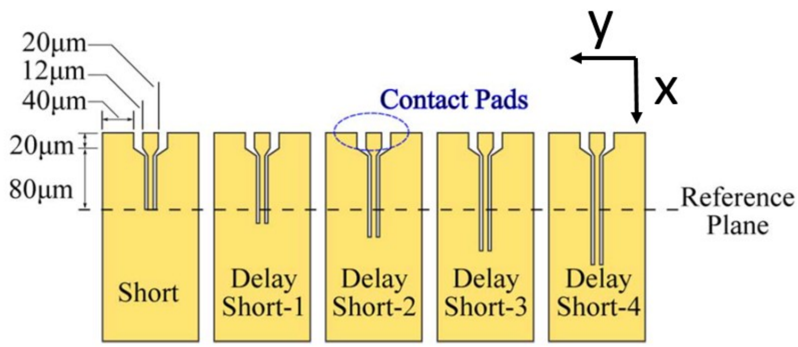

Figure 3.4: Dimensions of CPW calibration standards [44].

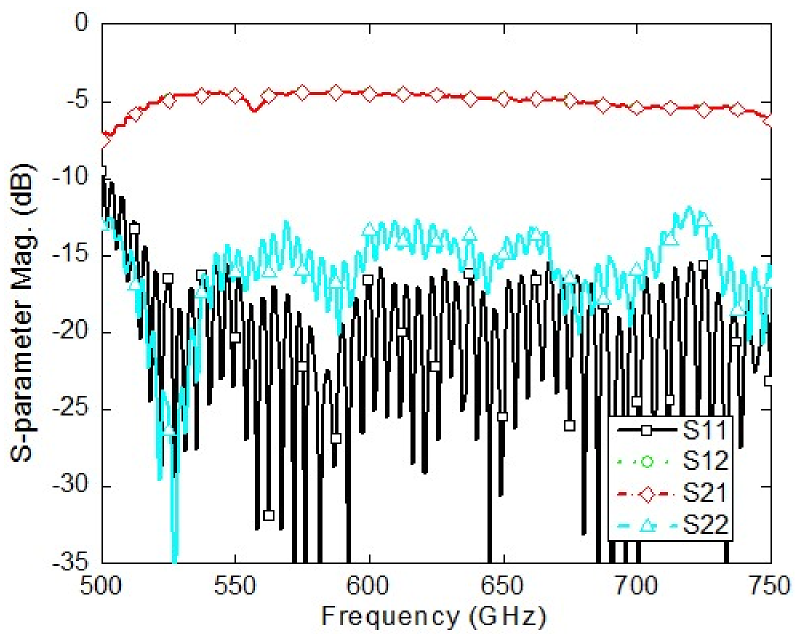

Figure 3.5: Average magnitude of S-parameters of WR-1.5 probe from 10 independent measurements.

3.2.1 Source Uncertainty

To study the effect of source uncertainty on the measurement uncertainty, the stage error and contact force variation need to be excluded from the measurement. First, the effect of source uncertainty on the delayed short is studied. In this experiment, the probe is landed on one of the delayed shorts (DS-2) with 20 mN contact force for 5 minutes. Raw data of S_{11} is taken every 10 seconds. The duration is chosen based on the time needed to complete 10 probe calibrations on one calibration set. The interval is chosen based on the time between measurements of adjacent delayed shorts. The relative standard deviation of

S_{11} for the measurement of DS-2 is plotted in Figure 3.6, which indicates the effect of source uncertainty on the delayed short. The average value of the relative standard deviation of S_{11} is summarized in Table 5.

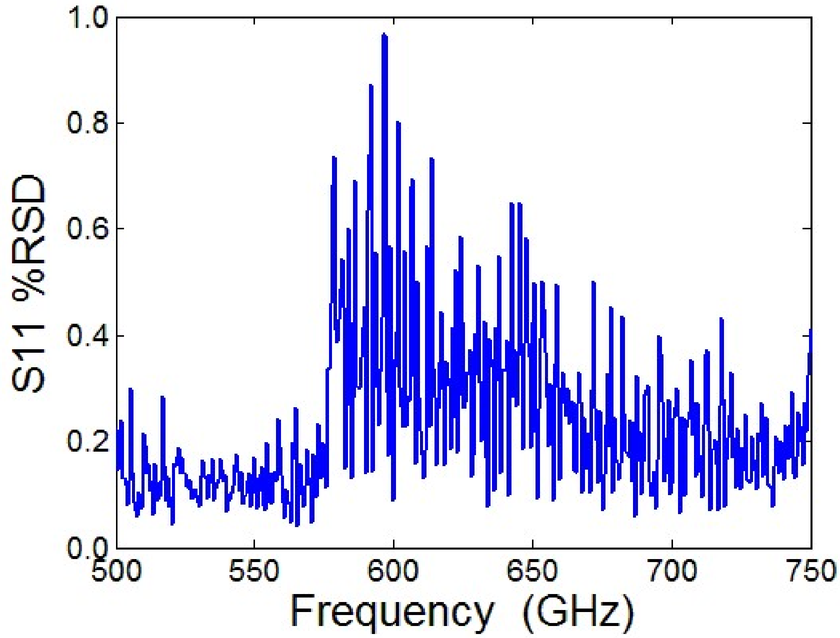

Figure 3.6: The relative standard deviation of S_{11} (raw) of DS-2.

Table 5: The average relative standard deviation of S_{11} for delay short DS-2.

Frequency (GHz)	500-575	575-650	650-750
RSD (%)	0.13	0.37	0.22

The effect of source uncertainty on the S-parameters of the probe can be simulated using the measurement results of the delayed short. The average relative standard deviation of DS-2 is used to simulate the effect of source uncertainty on the probe calibration. Recall that the probe S-parameters are calculated based on the raw S-parameters of 5 delayed shorts. The source uncertainty is added to the S-parameter of each delayed short in the following method (625 GHz is used for demonstration). Firstly, an average of 10 raw S_{11} of each delayed short from the single calibration set measurement is calculated and plotted in the complex plain. Then four additional points are selected randomly (both phase and magnitude) around each S_{11} at 625 GHz, with a relative distance of 0.25% (based on the data shown in Figure 3.6). Hence, for each delayed short, five possible values of raw S_{11} are generated for simulation based on the source uncertainty of the system. This process is illustrated in Figure 3.7 (data shown for 625 GHz). A Monte Carlo simulation is performed for each frequency within the WR-1.5 band using all possible combinations of the 5×5 raw S-parameters to obtain a set of probe S-parameters (3125 in total). The standard deviation of the simulated probe S_{21} is plotted in Figure 3.8.

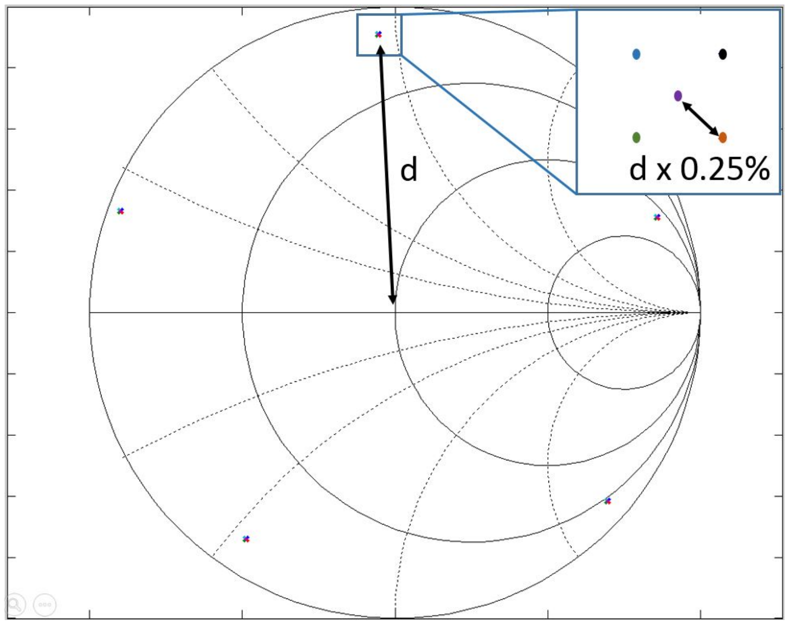

Figure 3.7: A illustration of the Monte Carlo simulation (@625 GHz).

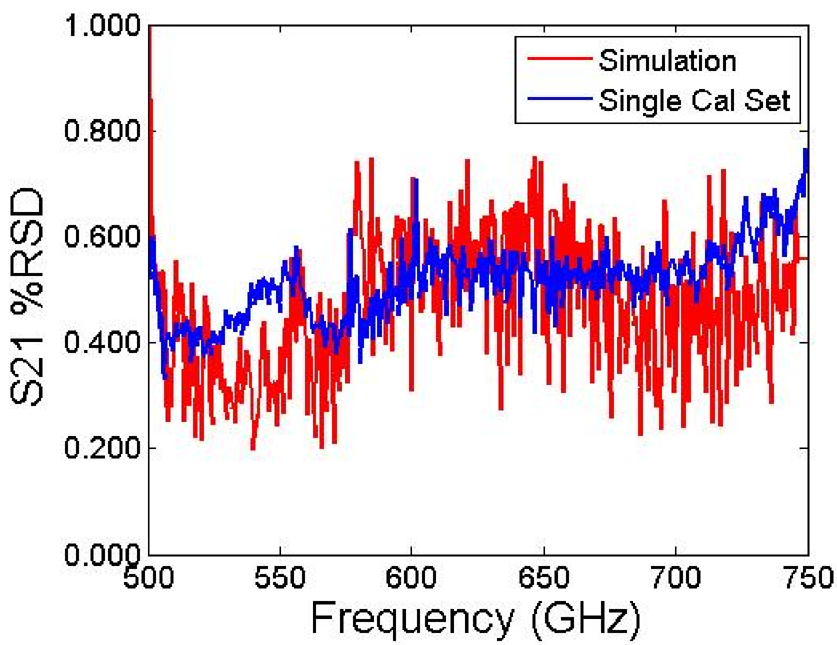

Figure 3.8: The relative standard deviation of probe S_{21} of Monte Carlo simulation and 10 independent measurements on one set of calibration standards.

To compare the simulated results with actual measurement data, 10 independent measurements (probe calibrations) with contact force controlled by the strain sensors on one set of calibration standards are performed. Measurement results are also plotted in Figure 3.8 as a comparison. As can be seen, the simulation agrees with measurement results within one calibration set due to the accurate force control provided by the strain sensor and the minimization of position errors within one set of calibration standards. Using the integrated strain sensors, the probe is angularly aligned to the test substrate within $\pm 0.025°$. A 20 mN contact force with ± 0.1 mN accuracy is achieved for the probe measurements, i.e., the z-travel for each contact is adjusted until the output of the strain sensor corresponds to 20 mN. Thus, the effect of contact force variation is minimized by the use of the integrated strain sensors. Limiting the measurements to one calibration set minimizes the stage error due to its accuracy (± 1.5 μm) and repeatability (± 1.0 μm). To complete the repeated probe calibration, only small y-direction movements are necessary, which have less significant impact on the measurement uncertainty compared to the x-direction movements (x- and y-direction as indicated in Figure 3.4). To illustrate this difference in sensitivity between x and y variations, a simulation is done for the case that the center probe tip is landed on the center of the contact pad, as well as for cases that the landing position is moved by 1.5 μm in x- and y-direction. Figure 3.9 shows how much the S_{21} of the probe deviates from the center contact in percentile. From the results shown in Figure 3.9, the x-direction movement uncertainty is the major factor in the measurement uncertainty contributed by the stage. As the position error increases, the difference between x- and y-direction deviation becomes more significant.

Since the effects of contact force variation and stage errors are both minimized in repeated measurements done at one calibration set, the effect of source uncertainty can be presented by the measurements using one calibration set (as shown in Figure 3.8).

3.2.2 Contact Force Variation

A typical 2-inch wafer has a thickness variation of 5 to 10 μm depending on its grade and vendors' specification, which can lead to 5 to 10 mN variation in contact force for a probe with 0.96 mN/μm spring constant given a fixed z-travel. Such variation in contact force caused by fixed z-travel leads to position error when measuring devices at locations of

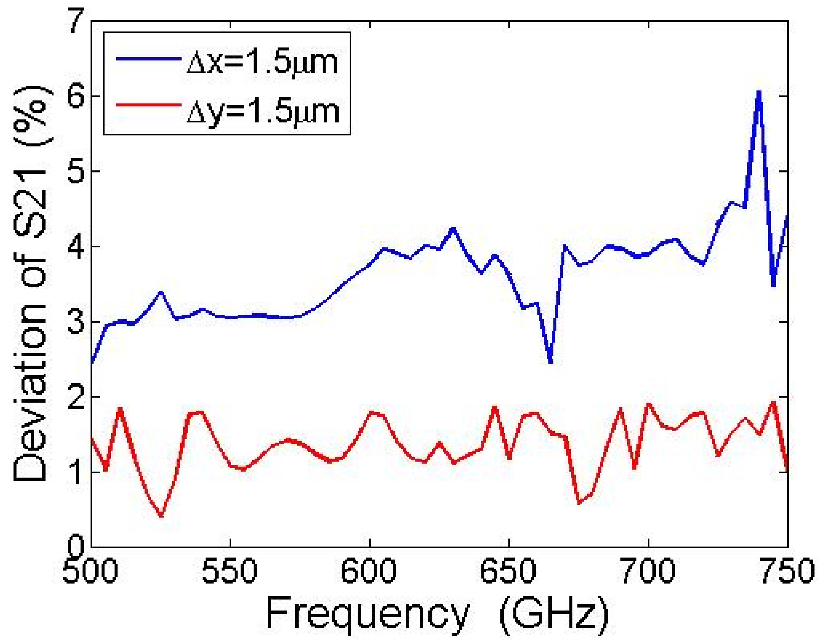

Figure 3.9: The simulated deviations of probe S_{21} from center contact

different thicknesses due to skating of the probe tip. To resolve this problem, a z-profiling method was developed by Cascade Microtech, Inc. to find the average optical height of selected positions on the wafer by focusing the microscope [77]. Z-travel for different devices can be corrected according to the wafer thickness profile. Hence, the position error can be reduced by z-profiling.

However, the contact force variation is also affected by the z-travel repeatability of the stage (± 1.0 μm, ± 0.25 μm resolution), which cannot be compensated by the z-profiling function. Using integrated strain sensors for large wafer probing is considered the optimal method due to its accurate contact force control which minimizes position error at the probe contact location and eliminates the effect of z-travel accuracy and repeatability.

A 2-inch wafer with multiple sets of CPW calibration standards (1.5 μm plated gold) as shown in Figure 3.4 is prepared. To study the measurement uncertainty of different methods for monitoring the probe contacts, 10 sets of calibration standards at different locations on the 2-inch wafer are measured (shown in Figure 3.1). Firstly, the planarity is adjusted by a bubble level (around $\pm 0.15°$ accuracy) and the initial contact is visually decided using a microscope image. To obtain a nominal contact force of 20 mN, a fixed z-travel of 15 μm beyond the initial contact is used for all sets of calibration standards when contacting the test pad of each CPW line. Due to the way initial contact is set (observing probe tip movement while raising the stage), a 0 μm z-travel associates with 3 to 5 mN contact force. For fixed z-travel, the relative standard deviation of S_{21} of the probe is between 6% and 8% for frequencies above 550 GHz (plotted in Figure 3.10).

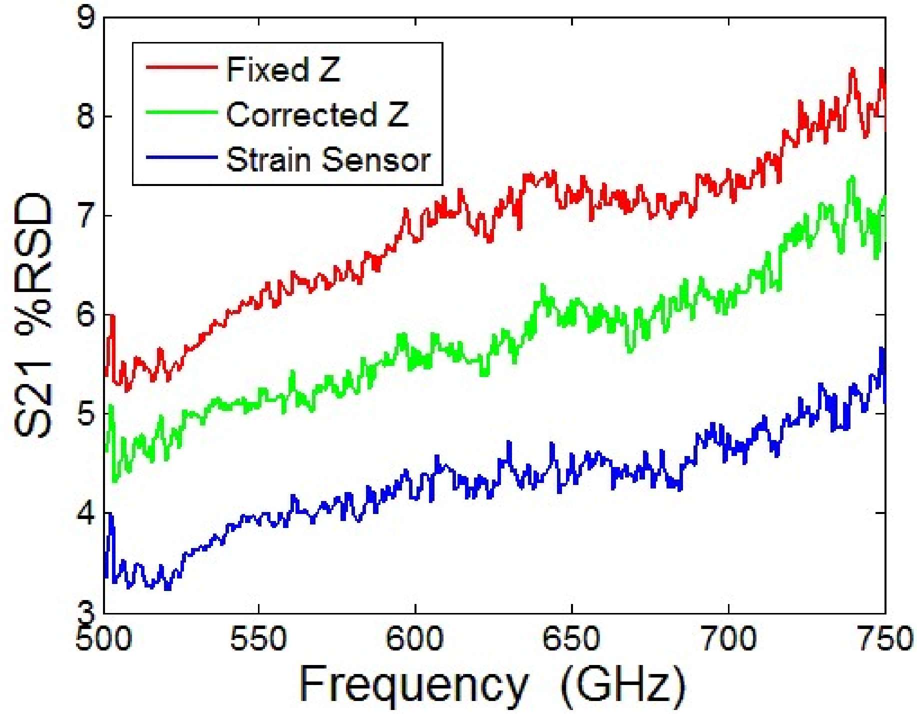

Figure 3.10: The relative standard deviation of S_{21} of the probe using different probe contacting methods.

Using the z-profiling function provided by the probe station (with an objective of 10× magnification and 0.28 numerical aperture), the relative height of each calibration set is measured with respect to the initial contact. The surface is assumed flat within the same calibration set. The z-travel for each contact is corrected based on the wafer thickness profile during the probe measurements to achieve a constant contact force across the wafer. Hence, the position error introduced by the skating variation is reduced. For example, if the lowest position on the wafer is -5 μm (initial contact 0 μm), to achieve a 11 mN contact force for a probe with 0.96 mN/μm spring constant, the z-travel at the lowest position needs to be 5 μm more than the reference position. As expected for this corrected z-travel, a smaller standard deviation for S_{21} of the probe is observed and plotted in Figure 3.10. For frequencies above 550 GHz, the relative standard deviation is between 5% and 7%.

Using the integrated strain sensors, a 20 mN contact force with ±0.1 mN accuracy is used for the probe measurements. As shown in Figure 3.10, the relative standard deviation of S_{21} of the probe is the lowest among all three methods. For frequencies above 550 GHz, the relative standard deviation is between 4% and 5%. In addition, an accurate wafer thickness profile is recorded from the z-travel for each calibration set.

The average error in z-profiling measurement is 1.8 μm with respect to the strain sensor measurement. During the z-profiling, the software is searching for a sharp microscopic image in a viewing area of 1500 μm $\times$ 1500 μm as the stage is moving up or down at a certain location. Any position within the depth of focus is considered acceptable. The corresponding optical height is then recorded. This mechanism causes the error in the wafer profile measurement. Using an objective of higher magnification and smaller depth of focus can reduce the error in the z-profiling measurement. However, the z-travel repeatability of the stage can not be compensated by an improved objective.

Note that the effects of source uncertainty and stage error are not excluded from the results shown in Figure 3.10. However, the contact force variation across the wafer has a significant impact on the on-wafer measurement accuracy and precision which is demonstrated clearly without the elimination of the other two factors. With correct z-travel for each contact, the measurement repeatability can be significantly enhanced. However, for operation without integrated strain sensors, wafer surface profiling should be performed to reduce measurement uncertainty. Considering the tolerance of planarization adjustment, a minimum of 5 mN contact force should be used for all probe contacts to compensate any potential angular misalignment. It is recommended to measure the spring constant of the probe prior to RF measurement and set the z-travel corresponding to the desired contact force.

3.2.3 Probe Contact Model

To further substantiate the effect of contact force variation on measurement uncertainty, the measurement of one delayed short is studied. The initial probe contact position is set to near the center of the contact pad. Thus, the part of the contact pad after the contact point can be treated as an open stub [44]. Changing the probe contact force is essentially changing the length of the delayed short and the open stub. In addition, the parasitic capacitance of the CPW open end extends the length of the open stub by approximately 11 μm [78]. This length is calculated using the following equation

$$l_{oc} = \frac{(S + 2W)}{4} \tag{3.1}$$

where l_{oc} is the effective length extension, S is the width of the signal line, and W is the width of the gap between signal line and ground. The CPW short-end inductive effect is considered as in Section 2.3.6 [68], [69]. As shown in Figure 3.4, the value of S and W are 20 μm and 12 μm, respectively. Note that for this analysis, the tapering between the contact pad and the CPW line are treated as a 50 Ω CPW line, which provides adequate accuracy. Figure 3.11 shows a diagram of the probe contacting a delayed short and the model used to simulate the effect of contact force variation. Simulation results of the phase difference for Delay Short-2 (DS-2) between 3 mN and 11 mN contact force is plotted in Figure 3.12. The physical lengths of the open stub for 3 mN and 11 mN contact force are assumed to be 3 μm and 6 μm. The skating can be estimated using the contact force, the spring constant of the probe (0.96 mN/m), and the length of probe extending beyond the waveguide block (400 μm). Assuming a straight probe beam during contact should provide sufficient accuracy of the skating distance. The following experiment is conducted to verify this model. An on-wafer calibration is done using 11 mN contact force to set the reference plane as shown in Figure 3.4 and then de-embedded to the probe tip [44]. 10 independent measurements of DS-2 in the same calibration set are done using 3 mN contact force. The same measurements are repeated using 11 mN contact force. Using the average phase of DS-2 measured at 11 mN as a reference, the phase difference of DS-2 between measurements using 3 mN and 11 mN contact force with standard deviation error bars is plotted in Figure 3.12. As can be seen for a contact force variation of 8 mN, the phase of a DS-2 can vary by up to 18° in the WR-1.5 band. The measurement result agrees with simulation, which proves the validity of the probe contact model.

3.2.4 Lateral Stage Accuracy and Repeatability

Another important factor of the measurement uncertainty is the lateral stage accuracy and repeatability. To study how the stage accuracy and repeatability influence measurement uncertainty, the effect of contact force variation at different locations are minimized by using the integrated strain sensors. 10 independent measurements using 20 mN force controlled

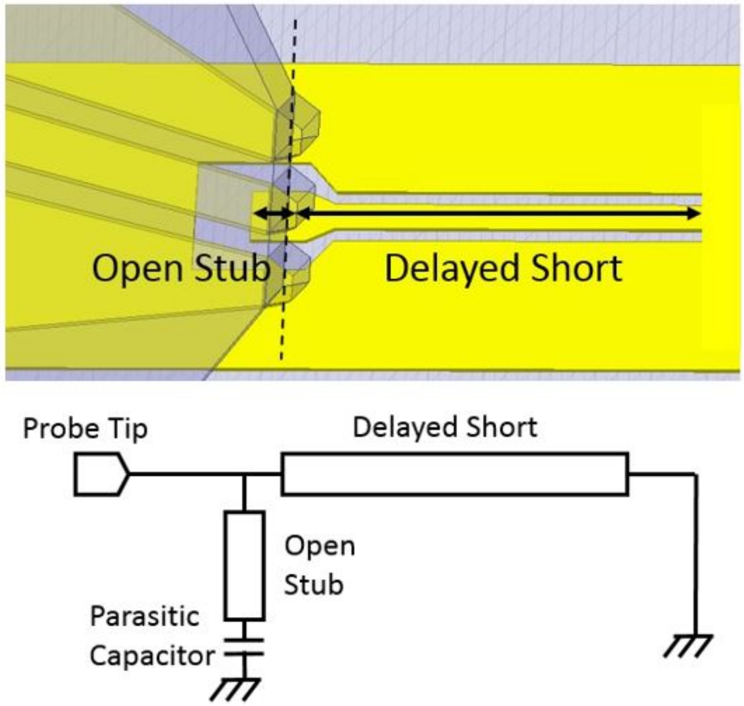

Figure 3.11: The diagram of the probe contacting a delayed short and the probe contact circuit model used to study the effect of contact force variation.

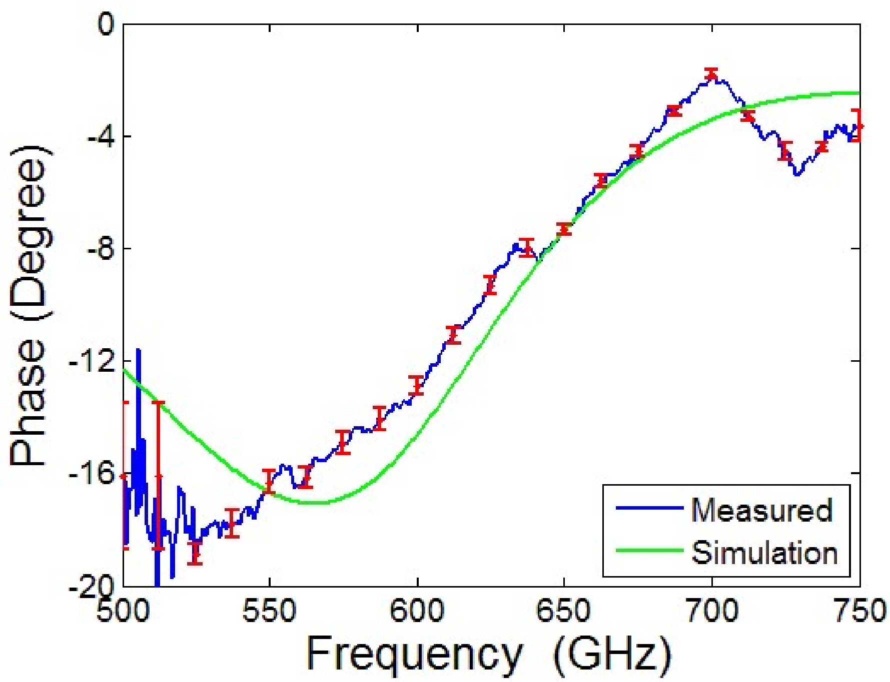

Figure 3.12: The measured and simulated phase difference of DS-2 between measurements using 3 mN and 11mN contact force.

by the strain sensors on a single set of calibration standards are performed. The relative standard deviation for S_{21} of the probe from this single set of calibration standards (shown in Figure 3.13) is used as a baseline to evaluate the effect of stage accuracy (± 1.5 μm) and repeatability (± 1.0 μm). The measurement results on 10 different calibration sets (as indicated in Figure 3.1) using 20 mN force controlled by the strain sensors are also plotted as a comparison. The measurement uncertainty within the same calibration set is reduced by approximately 90% compared to the result from multiple calibration sets. The rotational wafer alignment tolerance and the accumulated error of stage travel contribute to the deviation. This effect is simulated based on the data obtained from the single calibration set by adding position errors of 0.5 μm, 1 μm and 1.5 μm in probe contact positions. For each probe calibration, one out of ten random position errors within 0.5 μm, 1 μm and 1.5 μm is added to the short and four delayed shorts and a new S-parameter is calculated for each calibration standard using the probe contact model in Section 3.2.3. 10 new probe S-parameters can be calculated from the new S-parameters of the short and delayed shorts. The relative standard deviation of simulated S_{21} of the probe for position errors within 0.5 μm, 1 μm and 1.5 μm are plotted in Figure 3.13. For every 0.5 μm reduction in position error, the measurement uncertainty reduces by approximately one third.

3.2.5 The Effect of Position Errors in WR-1.0 Band

To emphasize the effect of position errors associated with the stage on higher frequencies, a similar simulation in the WR-1.0 band is performed based on 10 independent measurements on one calibration set. The S-parameter measurements are taken on the same test setup as in the WR-1.5 band, except with a one-port WR-1.0 frequency extension unit from Virginia Diodes Inc. (VDI WR1.0 VNAX113, 2 dBm RF, 5 dBm LO). To maintain a reasonable noise level and measurement time, decreased IF bandwidth (1 Hz) and number of points (41) are used. The same position errors (0.5 μm, 1 μm and 1.5 μm) are included in the simulation using the method introduced in Section 3.2.4 for the WR-1.5 band. The relative standard deviation of simulated and measured S_{21} of the probe are plotted in Figure 3.14. In the WR-1.0 band, the relative standard deviation of S_{21} of the probe is doubled comparing to the WR-1.5 band due to the larger source uncertainty. The effect of stage accuracy and repeatability shows significant influence on the measurement uncertainty.

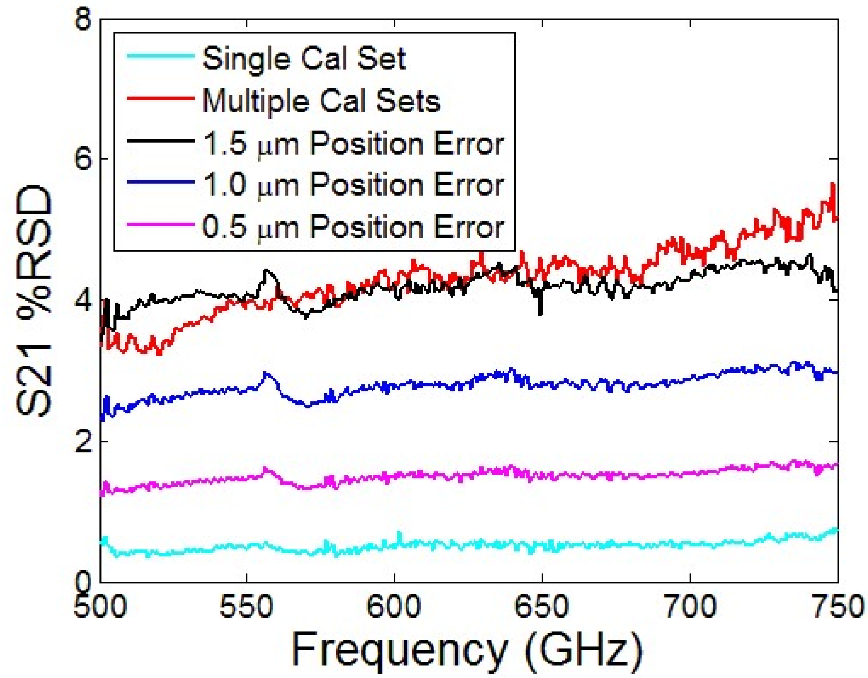

Figure 3.13: The measured (using single vs. multiple calibration sets) and simulated (with 0.5 μm, 1 μm and 1.5 μm position errors) relative standard deviation of S_{21} of the probe.

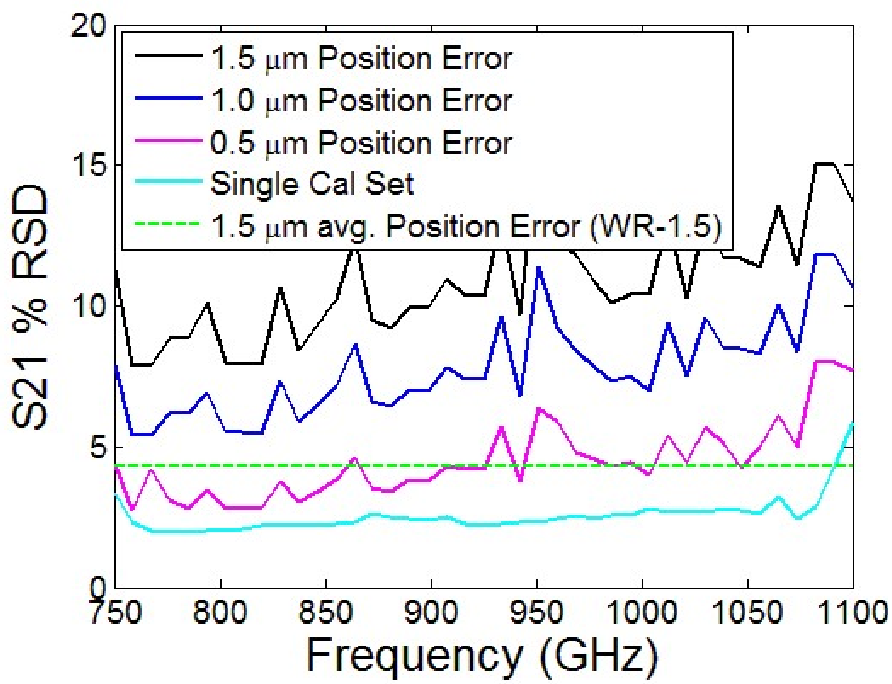

Figure 3.14: The simulated (with 0.5 μm, 1 μm and 1.5 μm position errors) relative standard deviation of S_{21} of the WR-1.0 probe.

3.2.6 The Effect of Position Errors from W-Band to WR-0.65 Band

To further demonstrate the effect of stage errors on probe measurement repeatability, a simulation is performed using the method introduced in Section 3.2.4 in expanded spectrum from W-Band (75 - 110 GHz) to WR-0.65 band (1100 - 1700 GHz). The same baseline measurements as in Section 3.2.4 (standard deviation of 10 independent measurements on a single calibration set in WR-1.5 band) are used for all bands in the simulation to represent the source uncertainty. The same position errors (0.5 μm, 1 μm and 1.5 μm) are included. Similar to the calibration standards used for WR-1.5 band (shown in Figure 3.4), the dimensions of the calibration standards for each band are determined by the center frequency. The relative standard deviation of simulated S_{21} of the probe are plotted in Figure 3.15. The grey area denotes the gap between W-band (75 - 110 GHz) and WR-5.1 (140 - 220 GHz). The dotted lines show the waveguide band designations. The discrepancies at the band edges are caused by the difference in the length of the calibration standards between different bands.

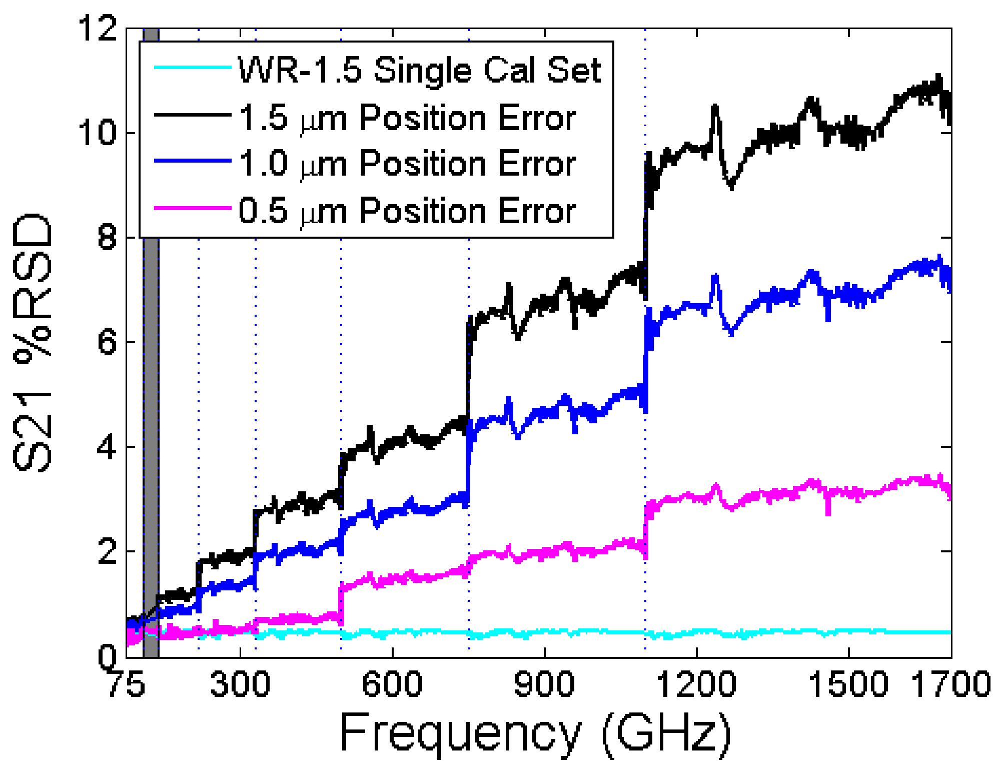

Figure 3.15: The simulated (with 0.5 μm, 1 μm and 1.5 μm position errors) relative standard deviation of S_{21} of the probe in expanded spectrum.

From results shown in Section 3.2.1, the baseline measurement is dominated by the source uncertainty due to the fact that it does not require any x-direction movement and has contact force controlled by the strain sensors. By assuming the same level of source uncertainty and only introducing position errors to each band, the effect of stage accuracy and repeatability becomes more and more apparent as frequency increases. Note that Figure 3.15 is an optimistic prediction for frequencies higher than 750 GHz. The reason is that the baseline measurements (standard deviation of 10 independent measurements on a single calibration set) is higher for the WR-1.0 band than the WR-1.5 band (results for higher frequencies unavailable due to equipment limitations). As shown in Figure 3.15, the effect of stage accuracy and repeatability should be even more significant in reality as frequency increases. From the results shown in Figure 3.13, Figure 3.14, and Figure 3.15, it is concluded that improving stage accuracy and precision will significantly reduce measurement uncertainty for on-wafer measurements beyond 500 GHz.

3.3 Summary

This chapter introduces the measurement uncertainty characterization of one-port large wafer probing in the WR-1.5 band. Factors that contribute to measurement uncertainty, including contact force variation, stage accuracy and repeatability, and the effect of source uncertainty, are discussed. Measurement results from a 2-inch wafer (on a probe station with 1.5 μm position error) indicate that using an integrated strain sensor to control the contact force achieves less than 5.5% worst case relative standard deviation (RSD) of the probe insertion loss in the WR-1.5 band. The measurement repeatability using the integrated strain sensor is better than using fixed z-travel (8.5% worst RSD) or using z-travel corrected by the z-profiling function of the probe station (7% worst RSD). The effect of wafer thickness variation on measurement uncertainty can be reduced by correcting z-travel using an integrated strain sensor or z-profiling function if strain sensor is unavailable. Simulated results show that for every 0.5 μm improvement in stage accuracy, the on-wafer probing measurement uncertainty for WR-1.5 band can be reduced by approximately 30%. Simulation results also show that the relative standard deviation will exceed 10% beyond 1200 GHz. Probe stations with improved stage accuracy and repeatability are desired to reduce the measurement uncertainty of THz on-wafer probing.

4 Micromachined Waveguide Components

4.1 Introduction

The rapid growth of millimeter and submillimeter–wave applications demands more precise measurements of waveguide components. Waveguide misalignment induced by flange is one of the major limitations to precise measurements above 110 GHz. Figure 4.1 shows the picture of maximum waveguide flange misalignment in different direction seen through waveguide shim [79].

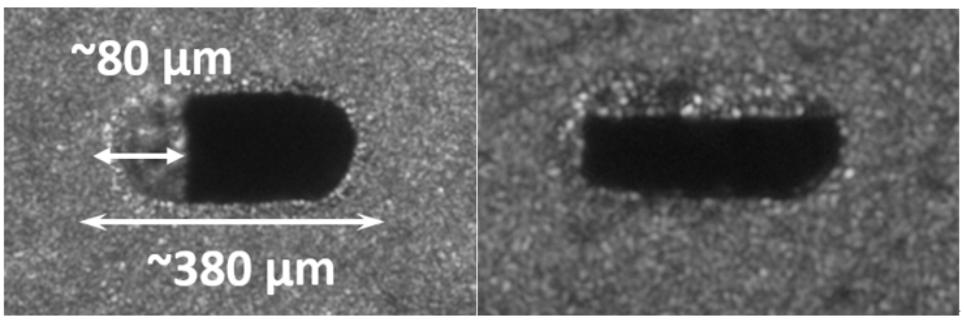

Figure 4.1: Waveguide flange misalignment creating maximum H-Plane and E-Plane offset [79].

In recent years, several efforts has been made to improve alignment and repeatability of the waveguide flange including Lau and Denning flange [80], Precision UG-387 with inner dowels [81] and ring-centered flange [82]. At present, the P1785 working group of the IEEE is considering multiple improved flange designs as standard rectangular waveguide interface. Results show that the improved ring-centered design (Figure 4.2) developed by H. Li et al. [83] provides higher repeatability than other candidates.

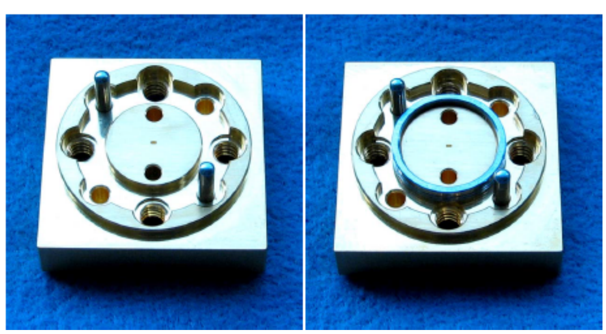

Figure 4.2: WR-2.2 ring-centered waveguide flanges [83].

In addition to the waveguide flange, measurement accuracy and precision are also affected by the quality of calibration standards, such as quarter-wave or eighth-wave calibration shims. Mismatch caused by waveguide tolerances, corner radii as well as flange misalignment leads to inaccurate calibration. Both conventional computer numerical control (CNC) milling and electric discharge machining (EDM) methods encounter imperfections in fabricated calibration shims due to the small waveguide dimensions for submillimeter-waves [84]. A typical shim fabricated by CNC milling is shown in Figure 4.3. It is clearly shown that the corners of the rectangular waveguide are significantly rounded. The effect of fabrication imperfection is shown in Figure 4.4a and 4.4b [84].

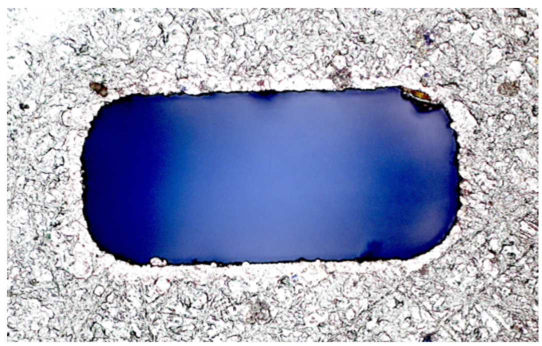

Figure 4.3: A typical calibration shim fabricated by CNC milling.

Another disadvantage of CNC milling and EDM is the inability to fabricate geometrically complex waveguide components. Figure 4.5 shows a 90° waveguide twist for WR-1.5 band, which is difficult to fabricate for both methods [76].

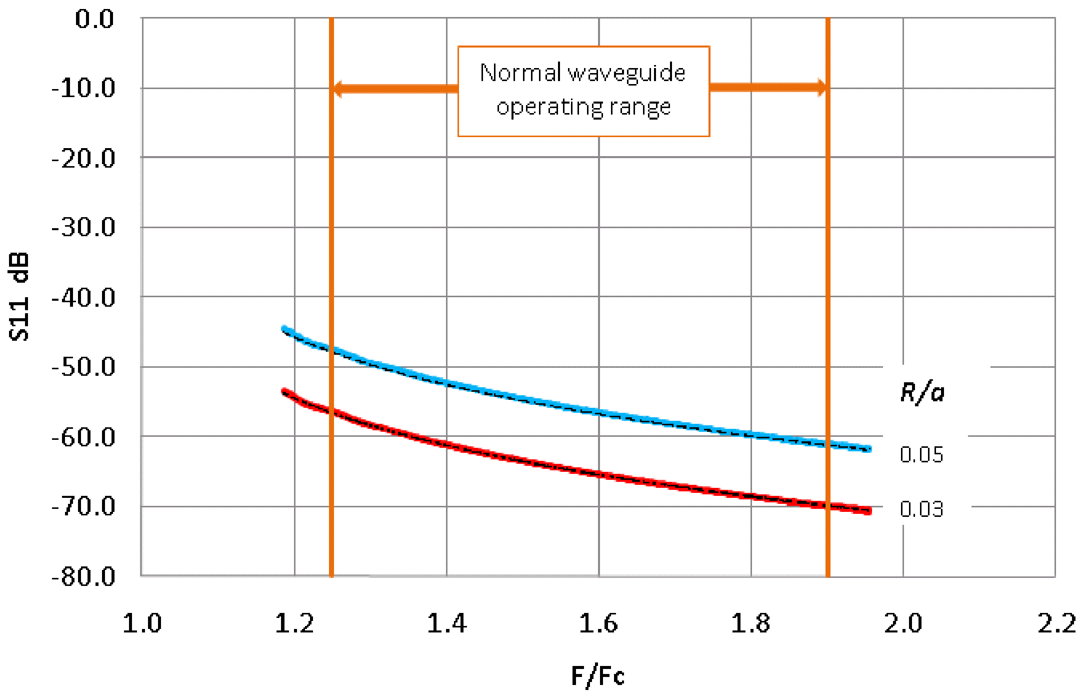

(a)

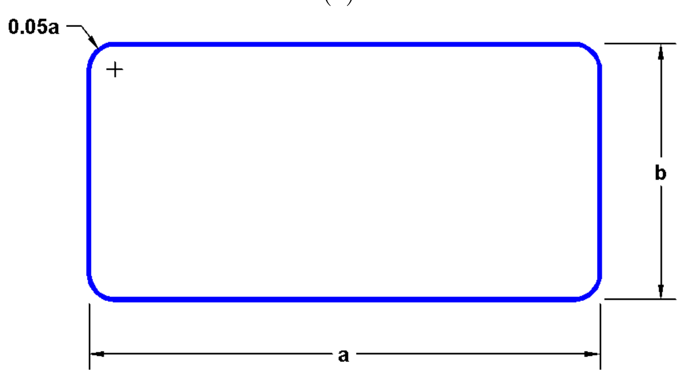

(b)

Figure 4.4: Mismatch caused by corner radii [84].

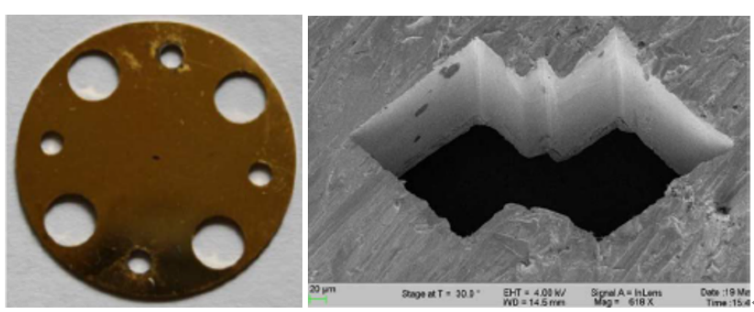

Figure 4.5: A microfabricated WR-1.5 band waveguide twist [76].

4.2 WR-2.2 Calibration Standard

Micromachining has been used in submillimeter-wave device fabrication for decades to overcome limitations associated with conventional machining techniques [85]. It has been shown to have the necessary precision to fabricate accurate submillimeter-wave circuits and structures that are impractical to fabricate using conventional machining [76], [86]. In this chapter an alternative fabrication approach for submillimeter- wave calibration standards using a KMPR based micromachining process is introduced. An accurate quarter-wave calibration shim for the WR-2.2 UG-387/UM waveguide flange is fabricated and characterized to validate this process. As a comparison, a quarter-wave WR-2.2 calibration standard for the same flange is prepared using the CNC milling method. Both shims are measured repeatedly to compare the results.

4.2.1 WR-2.2 Calibration Standard Fabrication Process

In our fabrication process, a negative photoresist, KMPR 1050, is selected due to its similarity to SU-8 in terms of applicable thickness and aspect ratio. Moreover it features certain improvements in adhesion to metals and removability. Firstly, a KMPR photoresist mold is built via photolithography on a silicon carrier wafer pre-coated with a titanium/gold/ titanium (10/50/20 nm) layer. The bottom titanium and gold are used as seed layers for electroplating. The top titanium later will be removed via reactive-ion etching once the mold is completed. Depending on the desired thickness, multilayer KMPR spin coating prior to lithography may be necessary. An SEM image and photograph of an example of the electroplating-mold are shown in Figure 4.6.

Then the whole mold is placed in boric-acid buffered nickel sulfamate solution at 50°C. The mold is typically over-plated by approximately 100 μm as the plating rate may vary across the surface. After electroplating, the plated sample is lapped and polished to the desired thickness. To release the shim from the substrate, the KMPR mold is removed via N-methyl-2-pyrrolidone (NMP) at 85°C for 15-30 min., followed by an overnight soaking in potassium hydroxide (KOH) at 110°C to remove the silicon carrier wafer. If any remaining KMPR is observed, an ultrasound soaking in de-ionized water may be applied to remove the residue. Finally, a thick layer of electroplated gold (approximately 1 to 2 μm) is applied

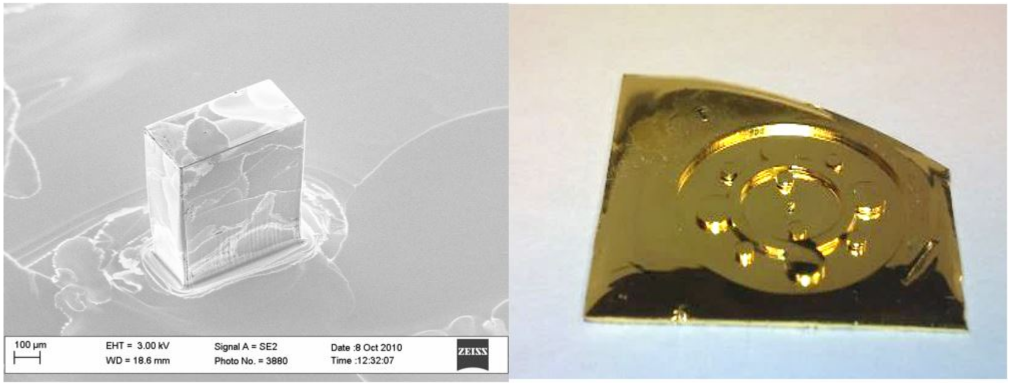

Figure 4.6: (left) SEM image of an electroplating mold (close-up of the waveguide mold); (right) photograph of an electroplating mold (top view).

to ensure that the thickness of gold exceeds the skin depth at the desired frequency (around 100 nm at 400 GHz). As a comparison, a WR-2.2 calibration shim for the same flange is prepared using the CNC milling method. Figure 4.7a, 4.7b show the SEM images and photographs of the fabricated shims.

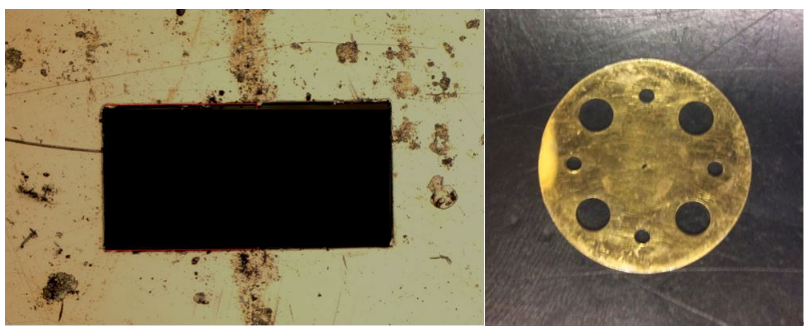

(a)

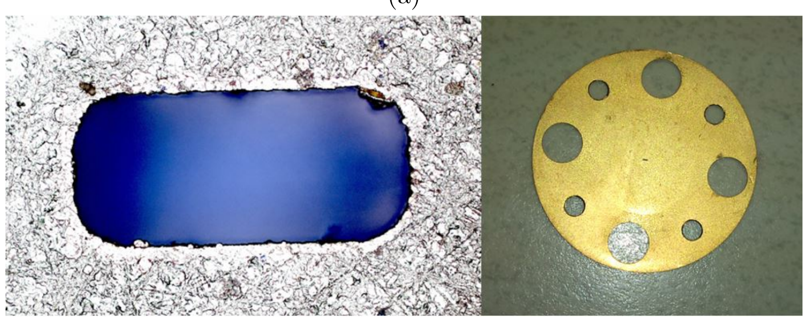

(b)

Figure 4.7: (a) - SEM image and photograph of the microfabricated and CNC quarter-wave calibration standards; (b) - SEM image and photograph of the microfabricated and CNC quarter-wave calibration standards

4.2.2 WR-2.2 Calibration Standard Measurements and Results

The shims are evaluated using a one-port WR-2.2 frequency extension unit from Virginia Diode Inc. (VDI WR2.2 VNAX-TXRX) and a Rohde and Schwarz ZVA-40 network analyzer. An open (delayed-short), short, match (OSM) calibration is done to a reference plane coincident with the frequency extension unit test port, using a flush short, a short with the microfabricated quarter-wave shim, and a precision load (return loss better than 50 dB). The same shim is inserted 10 times between the test port and the precision load in the same orientation as calibrated. Data is taken for each connection. The same measurements are repeated using the CNC shim. Measured return losses of both shims terminated with a match load are shown in Figure 4.8. Each trace is the average of 10 measurements. The S_{11} of the CNC shim is larger than the S_{11} of micromachined shim by approximately 5 dB due to the waveguide inaccuracy. To evaluate the measurement repeatability of both shims, an OSM calibration is performed for each shim prior to taking measurement results. In addition to the original shim orientation used during calibration (side A), the shims are also measured when rotated by 180° (side B), flipped by 180° about the E-field direction (side C), and both rotated and flipped by 180° (side D). S_{11} of 10 connections for each orientation are taken. The complex standard deviation of the measured results are used as a figure of merit of the measurement repeatability. The results for both shims in all four orientations are plotted in Figure 4.9a and 4.9b. The standard deviations of the microfabricated shim are between 0.003 and 0.008 for all four orientations, which is comparable to the CNC shim. The measurement results justify the fact that the designed diameter of the dowel holes on both shims are the same (63 mil). From the results in Figure 4.8, 4.9a, and 4.9b the microfabricated shim shows improved accuracy, comparable repeatability, and comparable variation when changing the connection orientation. Multiple shims from both fabrication methods are measured and show similar performance.

The waveguide dimensions are measured using Zeiss Axio Imager A1m microscope, with a 20× objective. The waveguide dimensions of the CNC shim are 578 μm × 273 μm (designed values are 559 μm × 279 μm, width × height). The average corner radius is 71 μm. The thickness is 258 ± 3 μm measured by Ono Sokki digital linear gauge EG-225. To evaluate the fabrication repeatability of the CNC method, the dimensions of 8 calibration shims (4 in WR-2.2 and 4 in WR-1.5) are measured. The standard deviation of the CNC process

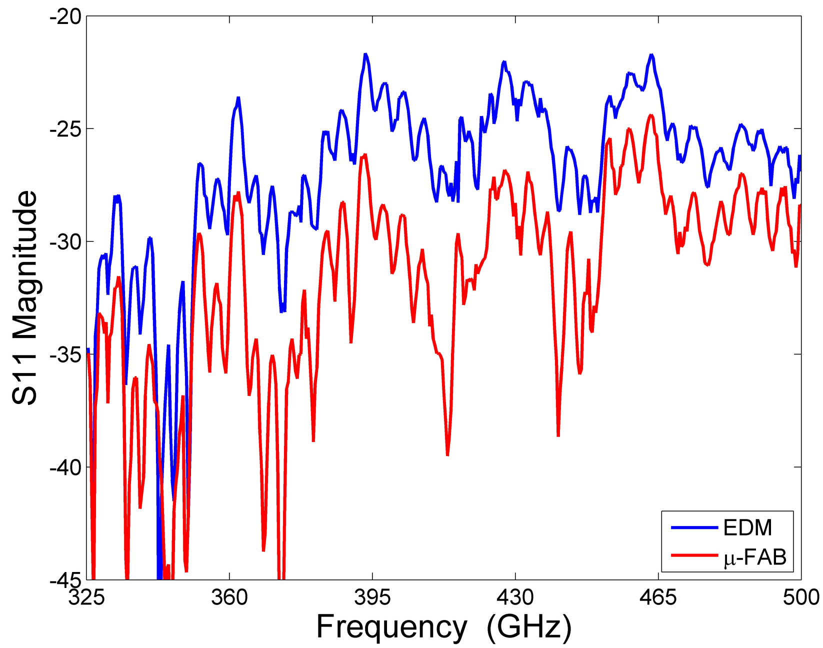

Figure 4.8: Return losses of fabricated shims terminated by precision load.

is around 6.0 μm. Note that the average dimensions of the CNC shims are off by 11 μm in width and -10 μm in height. For both shims, the waveguide dimensions of the two sides are different. When using the CNC method, the imperfection in milling bit causes the dimensional mismatch. When using KMPR, the bottom feature of the photo resist mold shrinks (shown in Figure 4.10), resulting in sidewall tapering [87]. Table 6 summarizes the difference in widths between top and bottom of fabricated waveguides of multiple thicknesses. After optimizing the lithography parameters, a tapered sidewall around 1.9° is observed in the photo resist mold. Hence, the same effect appears in the fabricated waveguide, which is essentially an opposite of the mold. On the top side, the dimensions of the waveguide are 561 μm $\times$ 279 μm, which are close to the designed values. On the bottom side, the waveguide dimensions scale down by 7 μm. The average corner radius is less than 10 μm. The thickness of the microfabricated shims are 205 $\pm$ 4 μm. The standard deviation of the top side waveguide dimensions of 8 WR-2.2 calibration shims is 4.3 μm. Table 7 summarizes the corner radius and standard deviation of both fabrication methods. It is concluded that micromachining features better accuracy of waveguide dimensions, smaller corner radius and improved fabrication process repeatability.

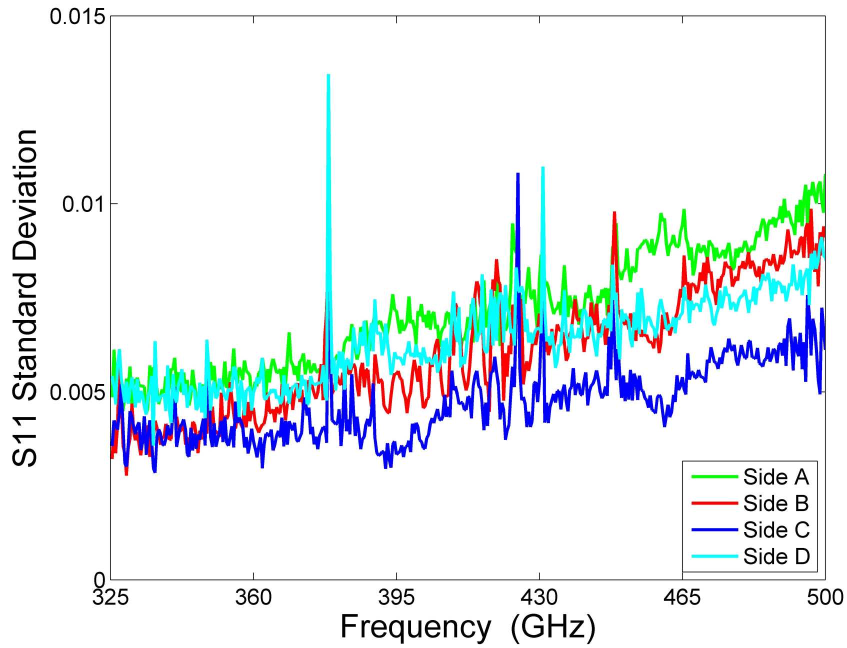

(a)

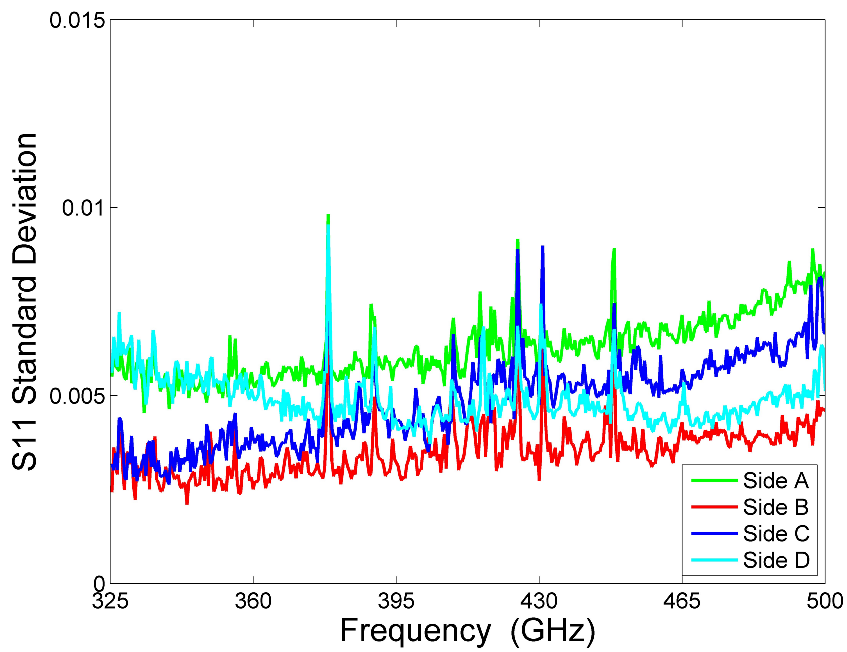

(b)

Figure 4.9: Complex standard deviation of S-parameters vs. frequency from 10 independent measurements - (a) CNC shim; (b) micromachined shim. Side A is the same orientation with calibration. Side B is rotated by 180° about the waveguide axis. Side C is flipped about the E-field direction. Side D is both rotated and flipped by 180°.

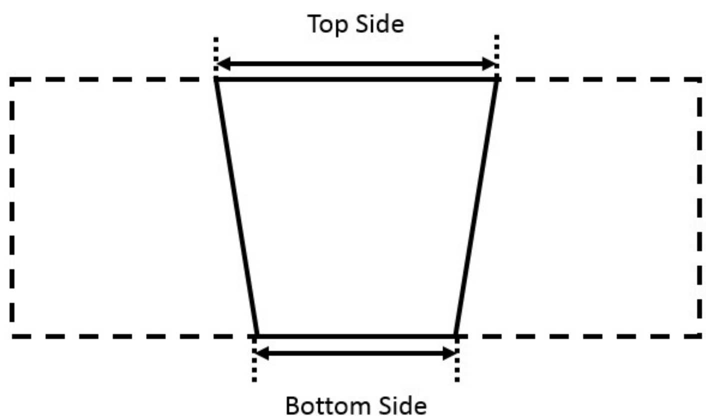

Figure 4.10: Demonstration of the waveguide tapering (exaggerated cross section).

Table 6: Measured Difference in Width between Top and Bottom of Fabricated Waveguides.

Micromachined Shim		CNC Shim	
Thickness (μm)	Width Difference (μm)	Thickness (μm)	Width Difference (μm)
430	11	258	18
205	7	204	8
170	5	114	5

Table 7: Corner Radius and Standard Deviation of Fabricated Waveguides.

	Micromachined Shim	CNC Shim
Corner Radius (μm)	Less than 10	71
Standard Deviation (μm)	4.3	6.0

4.2.3 Discussion

The accuracy of waveguide dimensions affect the quality of calibration. For frequencies beyond 500 GHz, the benefit of micromachining is substantial since the decreased waveguide dimensions require more accurate and repeatable fabrication techniques. This method is also extremely beneficial for the fabrication of submillimeter-wave devices having complex structures such as waveguide twists [76] and filters.

Five factors, linear misalignment, angular misalignment, corner radii, tapering in the rectangular waveguide, and dimensional mismatch (in width and height) contribute to the mismatch between the flange and the waveguide. Linear misalignment and dimensional mismatch are dominant among all. Assuming all other factors are ideal, the worst-case reflection coefficient (S_{11}) for a linear misalignment of 19 μm in the E-plane direction is around -30 dB, while the S_{11} for an worst-case angular misalignment of 0.57° is below -70 dB [84]. The S_{11} corresponding to the largest dimensional mismatch of 11 μm caused by the CNC milling is around -25 dB (2 μm for micromachining, S_{11} below -40 dB) [84]. The S_{11} corresponding to the corner radius of 71 μm caused by the CNC milling is around -25 dB (below -70 dB for micromachining, both simulated in HFSS 15.0) reflection of a tapered waveguide can be calculated based on the expression derived by R. C. Johnson in [88]. The micromachined shim yields an S_{11} below -90 dB, which is negligible compared to the reflection caused by the linear misalignment and the dimensional mismatch of the waveguide flange.

4.3 Summary

In this Chapter, an alternative fabrication approach for submillimeter-wave calibration standards using KMPR based micromachining process is introduced. This method overcomes limitations associated with conventional machining techniques. Taking advantage of the KMPR micromachining process, an accurate quarter-wave calibration shim for the WR-2.2 UG-387/UM waveguide flange is fabricated. As a comparison, a quarter-wave WR-2.2 calibration standard for the same flange is prepared using the CNC milling method. Measurement results show that the microfabricated shim features improved accuracy, small corner radius, and comparable repeatability. In addition, it is concluded that the micromachining method features better waveguide dimensions accuracy and improved fabrication process repeatability.

5 Conclusion and Future Work

In this work, two methods of using micromachined components to improve the accuracy and precision of submillimeter-wave measurement are presented.

5.1 Integrated Strain Sensor for THz Probing

The first method focuses on improving the repeatability and reliability of terahertz probing. The principle of this method is using symmetrical integrated strain sensor pair to monitor and control the contact condition of terahertz on-wafer probe. This method improves the repeatability of terahertz probing and enables accurate contact force measurement without modification to the standard probe station. Repeatable RF measurements can be achieved by aligning the probe tips angularly and controlling the contact force using the integrated strain sensors. By properly sensing and controlling the planarity of the terahertz probes, the required contact force can be significantly reduced to extend probe lifetime. Mechanical tests show that the integrated sensors have a contact force resolution of 0.2 mN and a contact angle resolution of 0.05° about the center. RF tests show that repeatable measurements can be achieved with 3 mN contact force after adjusting the probe contact angle within ±0.025° using the integrated sensors. For contact angle within ±0.15°, 5 mN contact force is sufficient to achieve repeatable measurements. In addition, measurement repeatability is also improved by angularly aligning the probe tips (reducing contact angle).

Taking advantage of this technique, measurement uncertainty of THz probing can be characterized. Factors that contribute to measurement uncertainty, including contact force variation, stage accuracy and repeatability, and the effect of source uncertainty, are analyzed. Measurement results from a 2-inch wafer indicate that using an integrated strain sensor to control the contact force achieves better measurement repeatability than using fixed z-travel or using z-travel corrected by the z-profiling function of the probe station. The effect of wafer thickness variation on measurement uncertainty can be reduced by correcting z-travel using an integrated strain sensor or z-profiling function if strain sensor is unavailable. Results show that stages of improved accuracy and repeatability are desired to reduce the measurement uncertainty of THz on-wafer probing. In addition, the recommended probe station specifications and procedure for THz probing without any integrated strain sensor are provided.

Future work includes the automated adjustment of both the contact force and angle for terahertz probing using the integrated strain sensors, which will enable the THz automated test environment (ATE) and greatly increase the test efficiency. In addition, based on the results from Chapter 3, for on-wafer measurements beyond 500 GHz, stage of improved accuracy and precision is in desire.

5.2 Micromachined Waveguide Components

The second method focuses on enhancing the accuracy of calibration by improving the quality of calibration standards (quarter-wave calibration shims). An alternative fabrication approach for submillimeter-wave calibration standards using KMPR based micromachining process is introduced. This method overcomes limitations associated with conventional machining techniques. The corner radii effect can be greatly reduced, which enables the fabrication of geometrically complex waveguide components, such as waveguide twist. Taking advantage of the KMPR micromachining process, an accurate quarter-wave calibration shim for the WR-2.2 UG-387/UM waveguide flange is fabricated. As a comparison, a quarter-wave WR-2.2 calibration standard for the same flange is prepared using the CNC milling method. Measurement results show that the microfabricated shim features improved accuracy, small corner radius, and comparable repeatability. In addition, it is concluded that the micromachining method features better waveguide dimensions accuracy and improved fabrication process repeatability.

Future work includes improving the efficiency of this technique and fabricating multiple shims on a larger wafer. Devices of new configuration are in development, such as waveguide twist consisted of multiple shims.

References

[1] M. J. Fitch and R. Osiander, "Terahertz waves for communications and sensing," *Johns Hopkins APL Technical Digest*, vol. 25, no. 4, pp. 348–335, 2004.

[2] P. Jepsen, D. Cooke, and M. Koch, "Terahertz spectroscopy and imaging – modern techniques and applications," *Laser and Photonics Reviews*, vol. 5, pp. 124–166, Jan. 2011.

[3] E. F. Federici, B. Schulkin, F. Huang, D. Gary, R. Barat, F. Oliveira, and D. Zimbars, "THz imaging and sensing for security applications explosives, weapons and drugs," *Semiconductor Science and Technology*, vol. 20, no. 7, pp. S266–S280, Jul. 2005.

[4] J. Xu and X. C. Zhang, "Terahertz technology and application," *Peking University Press*, pp. 230–246, Jul. 2007.

[5] C. Kulesa, "Terahertz spectroscopy for astronomy: From comets to cosmology," *IEEE Transactions on Terahertz Science and Technology*, vol. 1, no. 1, pp. 232–240, Sep. 2011.

[6] H. Song and T. Nagatsuma, "Present and future of terahertz communications," *IEEE Transactions on Terahertz Science and Technology*, vol. 1, no. 1, pp. 256–263, Sep. 2011.

[7] D. Etayo, J. C. Iriarte, I. Palacios, I. Maestrojuan, J. Teniente, I. Ederra, and R. Gonzalo, "THz imaging system for industrial quality control," *IEEE MTT-S International Microwave Workshop Series on Millimeter Wave Integration Technologies*, pp. 172–175, Sep. 2011.

[8] K. Yasuko, "Terahertz-wave remote sensing," *Journal of the National Institute of Information and Communication Technology*, vol. 55, no. 1, pp. 79–81, Mar. 2008.

[9] N. Vieweg, F. Rettich, A. Deninger, H. Roehle, R. Dietz, T. Gobel, and M. Schell, "Terahertz–time domain spectrometer with 90 dB peak dynamic range," *Journal of Infrared, Millimeter, and Terahertz Waves*, vol. 35, pp. 823–832, Oct. 2014.

[10] A. Roggenbuck, H. Schmitz, A. Deninger, I. Mayorga, J. Hemberger, R. Gusten, and M. Gruninger, "Coherent broadband continuous-wave terahertz spectroscopy on solid–state samples," *New Journal of Physics*, vol. 12, Apr. 2010.

[11] M. Nagai, H. Yada, T. Arikawa, and K. Tanaka, "Terahertz time–domain attenuatd total reflection spectroscopy in water and biological solution," *Interantional journal of Infrared and Millimeter Waves*, vol. 27, pp. 505–515, Apr. 2006.

[12] B. Fischer, H. Helm, and P. Jepsen, "Chemical recognition with broadband THz spectroscopy," *Proceedings of the IEEE*, vol. 95, pp. 1592–1604, Aug. 2007.

[13] K. Cooper, R. Dengler, N. Llombart, A. Talukder, A. Panangadan, C. .Peay, I. Mehdi, and P. Siegel, "Fast high–resolution terahertz radar imaging at 25 meters," *Proceedings of SPIE, Terahertz Physics, Devices, and Systems IV: Advanced Applications in Insdustry and Defense*, vol. 7671, pp. 169–182, Apr. 2010.

[14] S. Augustin and H. Hubers, "Phase–sensitive passive terahertz imaging at 5–m stand–off distance," *IEEE Transactions on Terahertz Science and Technology*, vol. 4, no. 4, pp. 418–424, Jul. 2014.

[15] J. Ding, M. Kahl, O. Loffeld, and P. Bolivar, "THz 3-D imaging formation using SAR techniques: simulation, processing and experimental results," *IEEE Transactions on Terahertz Science and Technology*, vol. 3, no. 5, pp. 606–616, Sep. 2013.

[16] E. Pickwell and V. Wallace, "Biomedical applications of terahertz thechnology," *Journal of Physics D: Applied Physics*, vol. 39, no. 17, pp. R301–R310, Sep. 2006.

[17] Y. Sim, K. Ahn, J. Park, C. Park, and J. Son, "Temperature–dependent terahertz imaging of excised oral malignant melanoma," *IEEE Transactions on Terahertz Science and Technology*, vol. 3, no. 4, pp. 368–373, Jul. 2013.

[18] Z. Taylor, R. Singh, D. Bennett, P. Tewari, C. Kealey, N. Bajwa, M. Culjat, A. Stojadinovic, H. Lee, J. Hubschmann, E. Brown, and W. Grundfest, "THz medical imaging: in vivo hydration sensing," *IEEE Transactions on Terahertz Science and Technology*, vol. 1, no. 1, pp. 201–219, Sep. 2011.

[19] C. Reid, G. Reese, A. Gibson, and V. Wallace, "Terahertz time–domain spectroscopy of human blood," *IEEE Transactions on Terahertz Science and Technology*, vol. 3, no. 4, pp. 363–367, Jul. 2013.

[20] E. Safrai, P. Ishai, A. Polsman, S. Einav, and Y. Geldman, "The correlation of ecg parameters to the sub–THz reflection coefficient of human skin," *IEEE Transactions on Terahertz Science and Technology*, vol. 4, no. 5, pp. 624–630, Sep. 2014.

[21] G. Stacey, "Terahertz low resolution spectroscopy for astronomy," *IEEE Transactions on Terahertz Science and Technology*, vol. 1, no. 1, pp. 241–255, Sep. 2011.

[22] A. Kerr, S. Pan, and W. Lyons, "The genesis of SIS mixers - the legacy of John Tucker in radio astronomy," in *2015 IEEE MTT-S International Microwave Symposium*, Phoenix, AZ, May. 2015.

[23] T. Kurner and S. Priebe, "Towards THz communications – status in research, standardization and regulation," *Journal of Infrared, Millimeter, and Terahertz Waves*, vol. 35, pp. 53–62, Aug. 2013.

[24] Study group on THz ICT at Kinki Bureau of Telecommunications, Ministry of Internal Affairs and Communications, Japan. Available: http://www.soumu.go.jp/soutsu/kinki/studygroup/2010/THz/index.html.

[25] J. Yao, R. Wang, H. Cui, and J. Wang, "Chapter 16: Atmospheric propagation of terahertz radiation," in *Remote Sensing - Advanced Techniques and Platforms*, InTech, Jun. 2012, pp. 371–386.

[26] Z. Zhu, S. Dong, and Y. W. adn Y. Dong, "A coherent detecting system of THz for the earth environment observation," in *2012 International Conference on Intelligent Sytems Design adn Engineering Application*, Sanya, China, Jan. 2012, pp. 963–966.

[27] J. Suen, M. Fang, and P. Lubin, "Global distribution of water vapor and cloud cover – sites for high–performance THz applications," *IEEE Transactions on Terahertz Science and Technology*, vol. 4, no. 1, pp. 86–100, Jan. 2014.

[28] M. Tonouchi, "Cutting-edge terahertz technology," *Nature Photonics*, vol. 1, pp. 97–105, Feb. 2007.

[29] R. Lewis, "A review of terahertz sources," *Journal of Physics D: Applied Physics*, vol. 47, no. 37, p. 374001, Jan. 2014.

[30] T. J. Reck, L. Chen, C. Zhang, A. Arsenovic, C. Groppi, A. Lichtenberger, R. M. Weikle, and N. S. Barker, "Micromachined probes for submillimeter-wave on-wafer measurements - part II: RF design and characterization," *IEEE Transactions on Terahertz Science and Technology*, vol. 1, no. 2, pp. 357–363, Nov. 2011.

[31] K. Topalli, G. Trichopoulos, and K. Sertel, "Non–contact probes for THz circuits and intergrated devices," in *2012 IEEE Antennas and Propagation Sciety International Symposium*, Chicago, IL, Jul. 2012.

[32] R. Lai, X. Mei, W. Deal, W. Yoshida, Y. Kim, P. Liu, J. Lee, J. Uyeda, V. Radisic, M. Lange, T. Gaier, L. Samoska, and A. Fung, "Sub 50 nm InP HEMT device with fmax greater htan 1 THz," in *2007 IEEE International Electron Devices Meeting*, Washington, DC, Dec. 2007, pp. 609–611.

[33] W. Deal, K. Leong, X. B. Mei, S. Sarkozy, V. Radisic, J. Lee, P. H. Liu, W. Yoshida, J. Zhou, and M. Lange, "Scaling of InP HEMT cascode integrated circuits to THz frequencies," *IEEE Symposium on Compound Semiconductor Integrated Circuit*, pp. 1–4, 2010.

[34] W. Deal and G. Chattopadhyay, "InP HEMT integrated circuits for submillimeter wave radiometers in earth remote snesing," in *2012 IEEE MTT-S International Microwave Symposium*, Montreal, Canada, Jun. 2012.

[35] P. Siegel, R. Smith, M. Gaidis, and S. Martin, "2.5–THz GaAs monolithic membrane–diode mixer," *IEEE Transactions on Microwave Theory and Techniques*, vol. 47, no. 5, pp. 596–604, May 1999.

[36] N. Alijabbari and R. Weikle, "A 200 GHz GaAs Schottky–diode phase shifter integrated on a silicon–on–insulater substrate," in *2013 IEEE MTT-S International Microwave Symposium*, Seattle, WA, Jun. 2013.

[37] N. Alijabbari, "Submillimeter–wave quasi–vertical GaAs schottky diodes integrated on silicon membranes," *Doctoral Dissertation*, p. 63, Aug. 2014.

[38] V. Radisic, K. Leong, X. B. Mei, W. Yoshida, and W. Deal, "Power amplification at 0.65 THz InP HEMTs," *IEEE Transactions on Microwave Theory and Techniques*, vol. 60, no. 3, pp. 724–729, Mar. 2012.

[39] C. Caglayan, G. Trichopoulos, and K. Sertel, "Device characterization with non–contact probes in the THz band," in *2013 US National Committee of URSI National Radio Science Meeting*, Boulder, CO, Jan. 2013.

[40] C. Caglayan, G. Trichopoulos, and K. Sertel, "Non–contact probe calibration for THz–frequency device characerization," in *2013 82nd ARFTG Mmicrowave Measurement Conference*, Coumbus, OH, Nov. 2013.

[41] C. Caglayan, G. Trichopoulos, and K. Sertel, "Non–contact probes for device and intergrated circuit characterization in the THz and mmW bands," in *2014 IEEE MTT-S International Microwave Symposium*, Tampa, FL, Jun. 2014.

[42] M. Moallem and K. Sarabandi, "A non–contact submillimeter–wave S–parameters measuremnt technique for multiport micromachined devices," *IEEE Transactions on Terahertz Science and Technology*, vol. 4, no. 3, pp. 338–346, May 2014.

[43] T. J. Reck, L. Chen, C. Zhang, C. Groppi, H. Xu, A. Arsenovic, N. S. Barker, A. W. Lichtenberger, and R. M. Weikle, "Micromachined on-wafer probes," *IEEE MTT-S International Microwave Symposium Digest*, pp. 65–68, 2010.

[44] L. Chen, C. Zhang, T. J. Reck, A. Arsenovic, M. Bauwens, C. Groppi, A. Lichtenberger, R. M. Weikle, and N. S. Barker, "Terahertz micromachined on-wafer probes: Repeatability and reliability," *IEEE Transactions on Microwave Theory and Techniques*, vol. 60, no. 9, pp. 2894–2902, Sep. 2012.

[45] M. Bauwens, L. Chen, C. Zhang, A. Arsenovic, A. Lichtenberger, N. Barker, and R. Weikle, "A terahertz micromachined on–wafer probe for WR–1.2 waveguide," in *Proceedings of the 7th European Microwave Integrated Circuits Conference*, Amsterdam, Netherlands, Oct. 2012, pp. 88–91.

[46] M. Bauwens, N. Alijabbari, A. Lichtenberger, N. Barker, and R. Weikle, "A 1.1 THz micromachined on–wafer probe," in *2014 IEEE MTT-S International Microwave Symposium*, Tampa, FL, Jun. 2014.

[47] Dominion Microprobes Inc., http://www.dmprobes.com/ProductsDMPI.html, Charlottesville, Virginia, 22905, USA.

[48] L. Chen, "Micromachined millimeter– and submillimeter–wave circuits for test and integration," *Doctoral Dissertation*, pp. 27–30, May. 2012.

[49] T. Reck, "Submillimeter wavelength metrology components," *Doctoral Dissertation*, pp. 23–27, Dec. 2010.

[50] F. Beer, R. Johnston, and J. DeWolf, *Mechanics of Materials*, The McGraw-Hill Companies Publishing, 1981.

[51] A. A. Barlian, W. Park, J. J. R. Mallon, A. J. Rastegar, and B. L. Prutt, "Review: Semiconductor piezoresistance for microsystems," *Proceedings of the IEEE*, vol. 97, no. 3, pp. 513–552, Mar. 2009.

[52] A. D. Kersey, T. A. Berkoff, and W. W. Morey, "Fiber-optic bragg grating strain sensor with drift-compensated high-resolution interferometric wavelength-shift detection," *Optics Letters*, vol. 18, no. 1, pp. 72–74, Jan. 1993.

[53] R. G. Azevedo, D. G. Jones, A. V. Jog, B. Jamshidi, L. C. D. R. Myers, X. Fu, M. Mehregany, M. B. J. Wijesundata, and A. P. Pisano, “A SiC MEMS resonant strain sensor for harsh environment applications,” *IEEE Sensor Journal*, vol. 7, no. 4, pp. 568–576, Apr. 2007.

[54] W. H. Ko, D. J. Young, J. Guo, M. Suster, H. Kuo, and N. Chaimanonart, “A high-performance MEMS capacitive strain sensing system,” *Journal of Microelectromechanical Systems*, vol. 15, no. 5, pp. 1069–1077, Oct. 2006.

[55] I. Kang, M. J. Schulz, J. H. Kim, V. Shanov, and D. Shi, “A carbon nanotube strain sensor for structural health monitoring,” *Smart Materials and Structures*, vol. 15, no. 3, pp. 737–748, Jun. 2006.

[56] J. M. Stephan, E. Pagounis, M. Laufenberg, O. Paul, and P. Ruther, “A novel concept for strain sensing based on the ferromagnetic shape memory alloy NiMnGa,” *IEEE Sensors Journal*, vol. 11, no. 11, pp. 2683–2689, Nov. 2011.

[57] R. A. Serway, “Principles of physics (2nd edition),” *Saunders College Publishers*, p. 602, 1998.

[58] I. H. Kazi, P. M. Wild, T. N. Moore, and M. Sayer, “Characterization of sputtered nichrome films for strain gauge applications,” *Thin Solid Films*, vol. 515, no. 4, pp. 2602–2606, Dec. 2006.

[59] M. A. Angadi and R. Whiting, “Longitudinal and transverse strain sensitivity of nichrome films,” *Materials Science and Engineering*, vol. 7, pp. L1–L4, Sep. 1990.

[60] J. Yan and J. Zhou, “Optimizing of strain sensitivity and electric characeristics of Ni–Cr thin film fabricatied by magnetron sputtering,” *Material Science and Technology*, vol. 23, no. 2, pp. 195–202, Feb. 2007.

[61] C. Smith, “Su–8 micromachining of millimeter and submillimeter–wave waveguide circuits,” *Master Thesis*, p. 86, 2008.

[62] J. Engel, J. Chen, and C. Liu, “Strain sensitivity enhancement of thin metal film strain gauges on polymer microscale structures,” *Applied Physics Letters*, vol. 89, no. 22, pp. 221 907–3, Nov. 2006.

[63] A. Singh, “Fabrication of a micro–hotplate for application as an infrared emitter,” *Master Thesis*, p. 56, 2015.

[64] I. H. Kazi, P. M. Wild, T. N. Moore, and M. Sayer, “The electromechanical behavior of nichrome (80/20 wt.%) film,” *Thin Solid Films*, vol. 433, no. 1–2, pp. 337–343, Jun. 2003.

[65] The State Education Department, “2006 Edition Reference Table for Physics Science Setting/Physics”, Albany, New York, 2006-2007.

[66] National Instruments, “Strain gauge measurementa tutorial”, National Instruments Application Note, no. 078, National Instruments Corporation, Austin, TX, Aug. 1998.

[67] Z. Liu and R. Weikle, "A reflectometer calibration method resistant to waveguide flange misalignment," *IEEE Transactions on Microwave Theory and Techniques*, vol. 54, no. 6, pp. 2447–2452, Jun. 2006.

[68] K. Beilenhoff, H. Klingbeil, W. Heinrich, and H. Hartnagel, "Open and short circuits in coplanar MMICs," *IEEE Transactions on Microwave Theory and Techniques*, vol. 41, no. 9, pp. 1534–1537, Sep. 1993.

[69] W. Getsinger, "End–effects in quasi–TEM transmission lines," *IEEE Transactions on Microwave Theory and Techniques*, vol. 41, no. 4, pp. 666–672, Apr. 1993.

[70] D. Buhl, "Molecular astronomy at submillimeter wavelengths," *Galactic and extragalactic infrared spectroscopy - Proceedings of the XVIth ESLAB Symposium*, vol. 108, no. 3, pp. 221–231, 1982.

[71] A. Arsenovis, L. Chen, M. Bauwens, H. Li, N. Barker, and R. Weikle, "An experimental technique for calibration uncertainty analysis," *IEEE Transactions on Microwave Theory and Techniques*, vol. 61, no. 1, pp. 263–269, Jan. 2013.

[72] L. Chen, C. Zhang, T. Reck, C. Groppi, A. Arsenovic, A. Lichtenberger, R. Weikle, and N. Barker, "Terahertz micromachined on-wafer probes: Repeatability and robustness," *IEEE MTT-S International Microwave Symposium Digest*, pp. 1–4, 2011.

[73] P. Walters, R. Pollard, J. Richardson, P. Gamand, and P. Suchet, "On-wafer measurement uncertainty for 3-terminal active millimeter-wave devices," *1992 IEEE GaAs IC Symposium Technical Digest*, pp. 55–58, Oct. 1992.

[74] J. Leinhos and U. Aze, "Monte–Carlo analysis of measurement uncertainties for on–wafer thru–reflect–line calibrations," *IEEE MTT-S International Microwave Symposium Digest*, pp. 33–36, Jun. 2008.

[75] V. Teppati and A. Ferrero, "A comparison of uncertainty evaluation methods for on–wafer S–parameter measurements," *IEEE Transactions on Instrumentation and Measurement*, vol. 63, no. 4, pp. 935–942, Apr. 2014.

[76] L. Chen, A. Arsenovic, J. R. Stanec, T. J. Reck, A. W. Lichtenberger, R. M. Weikle, and N. S. Barker, "A micromachined terahertz waveguide 90° twist," *Microwave and Wireless Components Letters*, vol. 21, pp. 234–236, May. 2011.

[77] Cascade Microtech, Inc., https://www.cmicro.com/news/cascade-microtech-s-nucleusandtrade–3-0-prober-control-software-provides-new-productivity-enhancing-tools-.

[78] N. Dib, "Comprehensive study of CAD models of several coplanar waveguide discontinuities," *IEEE Proceedings on Microwave and Antennas Propagation*, vol. 152, no. 2, pp. 68–76, Apr. 2005.

[79] H. Li, "Waveguide flange design and characterization of misalignment at submillimeter wavelengths," *Doctoral Dissertation*, Feb. 2013.

[80] Y. Lau and A. Denning, "An innovative waveguide interface for millimeter wave and submillimeter wave applications," Honolulu, HI, Jun. 2007.

[81] H. Li, A. Kerr, J. Hesler, and R. M. Weikle, “Repeatability of waveguide flanges with worst-case tolerances in the 500 – 750 GHz band,” in *79th ARFTG*, Montreal, Canada, Jun. 2012.

[82] A. R. Kerr and S. Srikanth, “The ring–centered waveguide flange for submillimeter wavelengths,” in *Proceedings of 20th International Symposium on Space THz*, Charlottesville, VA, Apr. 2009.

[83] H. Li, A. R. Kerr, J. L. Hesler, G. Wu, Q. Yu, N. S. Barker, and R. M. Weikle, “An improved ring–centered waveguide flange for millimeter– and sub–millimeter–wave applications,” in *76th ARFTG*, Clearwater Beach, FL, Dec. 2010.

[84] A. R. Kerr, “Mismatch caused by waveguide tolerances, corner radii, and flange misalignment,” *National Radio Astronomy Observatory Electronics Division Technical Note*, no. 215, Jan. 2010.

[85] D. Rutledge, “Micro-machining in submillimeter-wave circuits,” *IEEE MTT-S International Microwave Symposium Digest*, pp. 1889–1892, Jun. 1996.

[86] J. R. Stanec and N. S. Barker, “Fabrication and integration of micromachined submillimeter-wave circuits,” vol. 21, pp. 409–411, Aug. 2011.

[87] J. Stanec, “Micromachined components for submillimeter-waves,” *Doctoral Dissertation*, p. 21, May 2010.

[88] R. Johnson, “Design of linear double tapers in rectangular waveguide,” *IEEE Transactions on Microwave Theory and Techniques*, vol. 7, no. 3, pp. 374–378, Jul. 1959.

List of Figures

List of Tables

List of Publications

[1] **Q. Yu**, M. Bauwens, C. Zhang, A. W. Lichtenberger, R. M. Weikle, and N. S. Barker, "Improved micromachined terahertz on–wafer probe using integrated strain sensor," *IEEE Transactions on Microwave Theory and Techniques*, vol. 61, no. 12, pp. 4613–4620, Dec. 2013.

[2] **Q. Yu**, M. Bauwens, A. W. Lichtenberger, R. M. Weikle, and N. S. Barker, "Measurement uncertainty characertization of terahertz large wafer probing," in *International Microwave Symposium (IMS)*, Tampa, FL, Jun. 2014.

[3] **Q. Yu**, M. Bauwens, C. Zhang, A. W. Lichtenberger, R. M. Weikle, and N. S. Barker, "Integrated strain sensor for micromachined terahertz on-wafer probe," in *International Microwave Symposium (IMS)*, Seattle, WA, Jun. 2013.

[4] J. Do, **Q. Yu**, J. L. Hesler, and N. S. Barker, "A 330-500 GHz micromachined directional coupler," in *International Microwave Symposium (IMS)*, Seattle, WA, Jun. 2013.

[5] **Q. Yu**, J. L. Hesler, A. R. Kerr, H. Li, R. M. Weikle, and N. S. Barker, "Fabrication of calibration standards for the millimeter– and sub–millimeter wavelength ring–centered waveguide flange," in *77th ARFTG*, Baltimore, MD, Jun. 2011.

[6] H. Li, A. R. Kerr, J. L. Hesler, G. Wu, **Q. Yu**, N. S. Barker, and R. M. Weikle, "An improved ring–centered waveguide flange for millimeter– and sub–millimeter–wave applications," in *76th ARFTG*, Clearwater Beach, FL, Dec. 2010.

[7] M. Chudzik, I. Arnedo, I. Arreguii, F. Teberio, A. Lujambio, T. Lopetegi, M. Laso, **Q. Yu**, N. S. Barker, A. Ghaddar, A. Chahadih, G. Ducournau, J. Lampin, and T. Akalin, "Pulse shaping for millimeter–wave and terahertz applications in coplanar technology," in *Proceedings of the 44th European Microwave Conference*, Rome, Italy, Oct. 2014.

[8] A. Chahadih, S. Kaya, G. Moreno, M. Zeha, I. Turer, A. Ghaddar, **Q. Yu**, N. S. Barker, and T. Akalin, "Planar goubau lines with corrugated sections for controlling the terahertz waves," in *Les Troisiemes Journees France – Libanaises (JFL3)*, Oct. 2015.